Determining the Heterogeneous Properties of the Bladder Wall Using 3D-Analysis of the Whole Bladder

by

Ricardo José Cardoza

B.S. in Mechanical Engineering, University of Maryland Baltimore County, 2019

Submitted to the Graduate Faculty of the

Swanson School of Engineering in partial fulfillment

of the requirements for the degree of

Master of Science in Mechanical Engineering

University of Pittsburgh

2021

UNIVERSITY OF PITTSBURGH

SWANSON SCHOOL OF ENGINEERING

This thesis was presented

by

Ricardo José Cardoza

It was defended on

October 15, 2021

and approved by

Anne M. Robertson, Ph.D., Professor
Department of Mechanical Engineering and Material Science

Lori Birder, Ph.D., Professor of Medicine
Department of Medicine

Spandan Maiti, Ph.D., Associate Professor
Department of Bioengineering

Paul Watton, Ph.D., Senior Lecturer
Department of Computer Science at The University of Sheffield

Thesis Advisor: Anne Robertson, Ph.D., Professor
Department of Mechanical Engineering and Material Science

Determining the Heterogeneous Properties of the Bladder Wall Using the 3D-Analysis of the Whole Bladder

Ricardo José Cardoza, M.S.

University of Pittsburgh, 2021

The bladder is a highly compliant organ meaning it can experience large deformations without experience large pressures. Often, this compliance decreases as the bladder ages or experiences disease resulting in a loss of functionality. This loss of functionality can cause a decrease in quality of life of the affected individual therefore a further understanding of the mechanics of the bladder needs to be developed to better prevent and treat bladder issues. Research involving the bladder has been conducted mostly on segments using uniaxial and biaxial testing. Although these tests have set the foundation for bladder research, these tests do not address bladder heterogeneity in wall thickness of material properties. To address this gap in knowledge, in this thesis, the wall thickness and mechanical behavior of the intact bladder was studied. The bladder was first imaged using micro-CT. These scans provide geometric results for the bladder such as wall thickness and shape. This data, along with the pressure readings, were used to calculate the compliance. Next, the bladder was analyzed using digital image correlation which provides local strain results for the bladder. Finally, the strain was then used with a virtual field method to approximate the local shear modulus across the bladder surface. These tests were also conducted on bladders that have been treated with hypoxanthine to compare with the controls. This study showed that the bladder has heterogeneous material properties and wall thickness increases at the bottom of the dome. Strain is also shown to be higher at the dome and this results in a lower shear modulus compared to the urethra side. The study also showed that, on average, the treated bladder

has thinner bladder walls, greater volume and is more compliant than the control. These findings show that the location of the bladder specimen is significant when conducting research as one area could behave significantly different properties than another. Knowing this, more accurate research can be conducted on the bladder to further future advance in bladder treatment and care.

Table of Contents

List of Tables

List of Figures

Preface

During my time at the University of Pittsburgh, I had the honor to meet and work with so many amazing people who helped me develop into a greater researcher. I would like to thank all my colleagues in the lab for the assistance they provided in basic lab training to helping me run experiments when I had surgery. Thank you to Adrien Grimberg from Ecole des Mines de Saint-Etienne, the team from Correlated Solutions and IEE for allowing me to reproduce their figures in my thesis. I would also like to thank everyone in my committee for taking the time to be a part of this wonderful milestone in my life and for providing me feedback. Finally, I would like to thank my advisor, Dr. Anne Robertson, for this wonderful opportunity to work with her. She has been not only an amazing advisor, but an amazing support system for when things became difficult.

Along with the wonderful people from UPitt, this milestone would not have been possible without my family who always supported me throughout my journey. Le quiero dar gracias a mi novía Leslie Hernández quien, con su apoyo, tuve la fuerza para seguir luchando este año. A mis hermanos, quienes siempre han estado a mi lado durante lo mejor y lo peor. Y últimamente, a mi madre quien, toda mi vida, ha hecho todo lo posible para proveer me con las oportunidades que he tenido.

Finally, this year I unexpectedly lost my father, José Sergio Cardoza, due to covid. All the work I put into this thesis and my time at Pitt, I want to dedicate in his memory. Mi papa lucho hasta el final por su familia y con sus sacrificios, pudo cuidarnos y darnos oportunidades que el nunca tuvo. Era un hombre fuerte y el siempre ayudaba a sus amigos y a su familia. Yo no pudiera ser el hombre quien soy sin su amor y apoyo. Te amo papa y algún día te vere otra vez para

decírtelo. Tu fuiste el mejor padre que pude tener y te voy a orgullecer por ser mi padre como yo siempre seré orgulloso de ser tu hijo. Gracias por todo y siempre honrare tu memoria.

1.0 Introduction

The research conducted in this thesis serves to advance the knowledge and understanding of how the whole bladder behaves in contrast to most prior works where isolated sections are mechanically tested or evaluated using histological approaches. In this study, rat bladders, both treated and controls, are examined to determine their geometric and local material properties. Digital image correlation (DIC) is used to determine strain values and create a color map that shows the strain field as the bladder inflates. The geometry of the bladder is also examined using micro-CT imaging which allows for nondestructive analysis of the wall thickness and shape. Finally, the results from these tests are analyzed using an inverse approach which produces local stiffness values for the bladder. In addition to applications to animal studies, approaches used in this study can later be applied to human bladders and be a vital tool for understanding the loss of bladder functionality and guiding the development of new treatments.

1.1 Motivation

The human bladder is a highly compliant organ which can expand to hold up to 450 ± 64.4 ml of urine while only experiencing a transmural pressure of 43.5±7.3 cm of H_2O in in young adults (18 years old) [1]. Unfortunately, as a person ages or experiences disease, the bladder can become less effective due to a decreased compliance with an associated increase in voiding pressure [2]. Bladder compliance is defined by The International Continence Society as:

$$C = \frac{\boldsymbol{\Delta V}}{\boldsymbol{\Delta P}} \qquad \textbf{(1.1)}$$

Where $\boldsymbol{\Delta V}$ is the change in volume and $\mathbf{\Delta P}$ is the change in pressure.

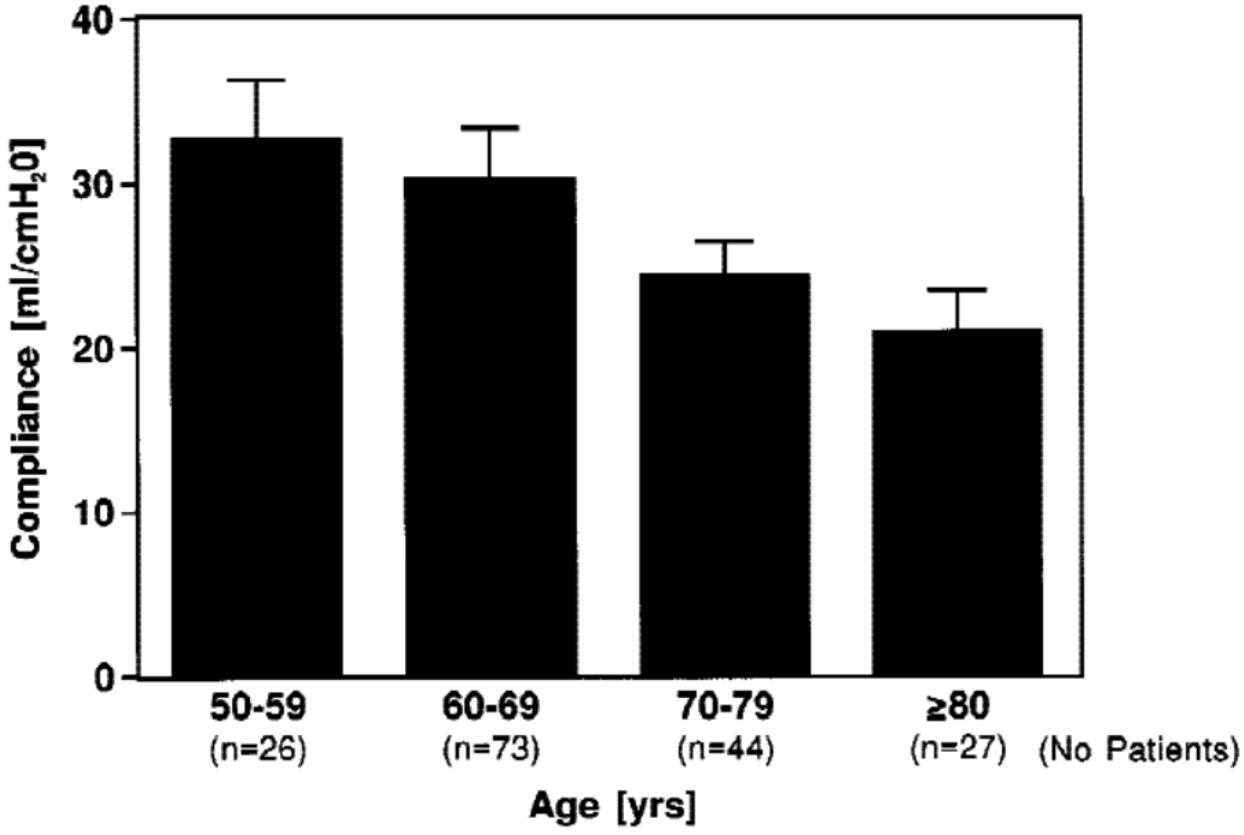

Figure 1 Age-related decrease in bladder compliance in elderly men with lower urinary tract symptoms.

(Reprinted from [3], with permission from John Wiley and Sons)

This loss of compliance can have serious health implications since the increase in pressure in the bladder can be transmitted to other organs, such as the kidneys, and may lead to infection, pain, and kidney failure [4]. Along with the bladder compliance, overactive bladder syndrome is a very common medical condition in older adults that affects quality of life as it causes an increase in urinary frequency, involuntary urination, and nocturia [5].

Although age and disease cause a decrease in compliance, there is another factor that can cause a decrease in bladder functionality in the bladder and that is spontaneous bladder contractions. These spontaneous contractions are involuntary and may cause urination by the

patient while also increasing pressure in the ureters which can lead to renal failure [6]. These contractions are primarily caused by the detrusor smooth muscle cells in the bladder wall.

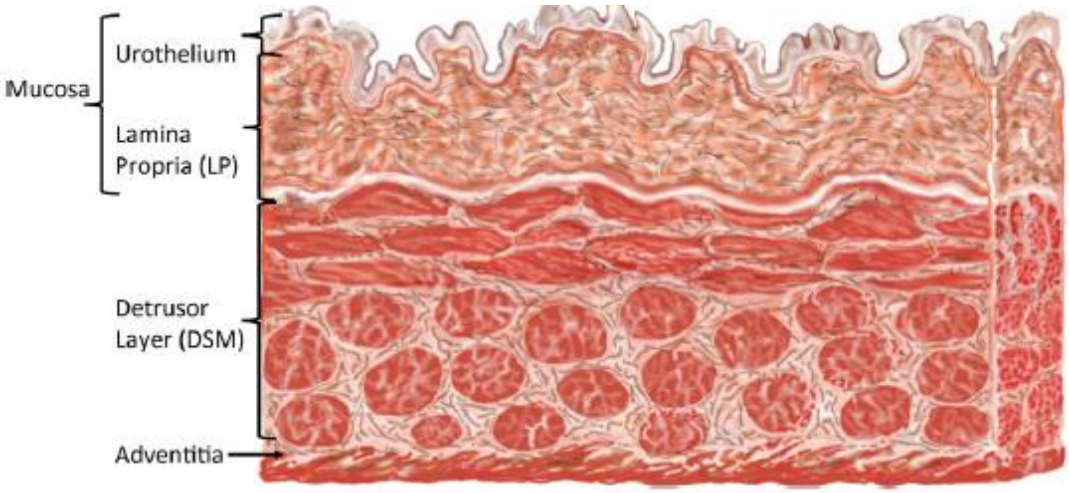

Figure 2 Schematic of a cross section of the bladder wall showing the three major layers (mucosa, detrusor smooth muscle layer and adventitia). The folds (rugae) of the mucosa layer involve both the urothelium and lamina propria layers. (Reprinted from [7], with permission from Springer Nature)

Knowing what the problems are that the bladder faces is a start but a deeper understanding of its mechanical behavior and heterogeneity must be developed. By looking at the bladder as a whole and obtaining values for these mechanical properties, more accurate research can be conducted on the bladder that could help develop new treatment for patients suffering from bladder issues.

1.2 Current Understanding of Bladder Wall Mechanics

The urinary bladder is a musculomembranous hollow organ that consists of several layers as shown in Figure 2. The bladder relaxes and contracts to allow for the storage and voiding of urine. There is still limited knowledge on the mechanobiological behavior of the bladder and so further analysis, and the use of novel testing methods are needed to understand more thoroughly the mechanics of this organ.

Current knowledge of the mechanics of the bladder wall is largely based on data from uniaxial testing and biaxial testing. However, these studies are mostly conducted with small strips or squares taken from whole bladders [9][10][11]. Taking segments from the bladder provides valuable insight to its behavior but generally assumes homogenous mechanical properties.

Finally, as previously mentioned, the bladder can experience spontaneous contractions that are not only present in damaged or aged bladders, but also healthy and young bladders. These contractions present an extra challenge in analysis of bladder biomechanics as they can alter force measurements as seen in Figure 3 where contractions were induced on a uniaxial tested strip of bladder and the resulting force-displacement data was compared to a control sample.

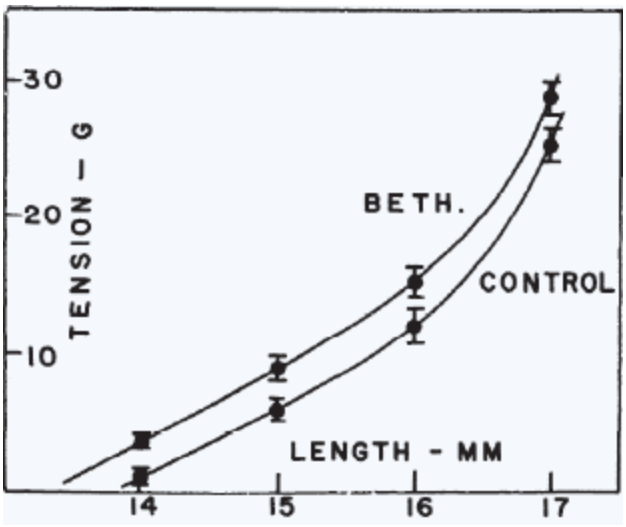

Figure 3 Force-deflection response of bladders with induced contractions using bethanechol chlorade compared to control samples (Reprinted from [8], with permission from The American Physiology Society)

1.2.1 Uniaxial Testing

In uniaxial testing, a rectangular or dog-bone shaped sample is clamped at two ends and pulled along the axial direction. In strain controlled experiments, the clamps are usually connected with load cells to measure the force applied, as a function of strain. A common setup for uniaxial testing is shown in Figure 4. In uniaxial testing, three specific phases have been noted for bladder tissue. First, there is a rapid viscoelastic extension, followed by a slower plastic creep and finally a more rapid creep if load is maintained for a sufficient period [8].

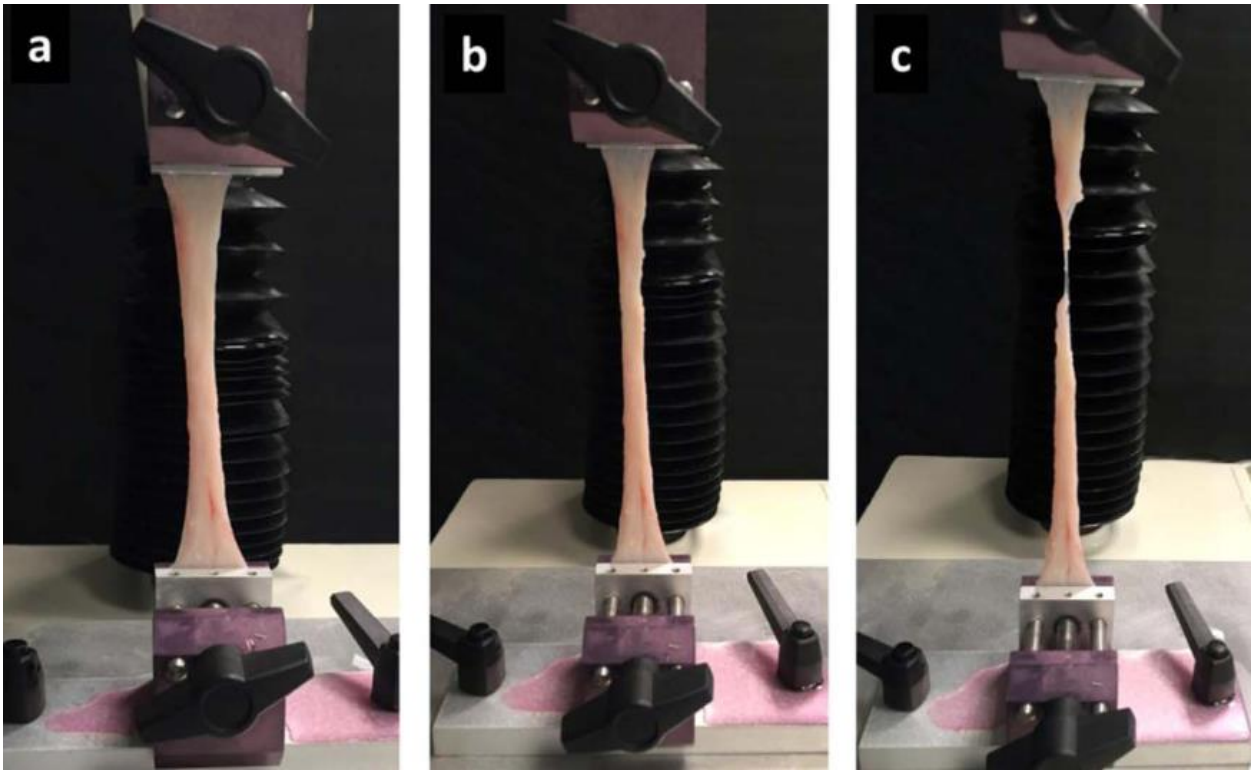

Figure 4 Unixial testing setup for porcine bladder testing. Sample loaded to rupture from a to c. (Reprinted from [23], with permission from Elsevier)

One of the most cited works in this field is a study from Dahms *et al*. In this study, uniaxial testing is performed on rat, pig, and human bladder tissue as well as its acellular matrix graft (BAMG). The aim of this study was to identify the ultimate tensile strain, ultimate tensile strength, and elastic modulus of bladder tissue to obtain a better understanding of the biomechanics. As it better pertains to the studies presented in this thesis only, the elastic modulus results of this study are shown in Table 1 [10].

Table 1 Mechanical properties of rat, pig and human bladder tissue and BAMG [10] *P < 0.05 vs. normal rat bladder (Reprinted from [10], with permission from John Wiley and Sons)

Material	Number of samples	Elastic modulus (MPa)
Rat BAMG	10	1.43 (0.58)*
Rat bladder	10	0.76 (0.44)
Pig BAMG	10	0.40 (0.13)
Pig bladder	10	0.26 (0.18)
Human BAMG	10	0.60 (0.21)
Human bladder	10	0.25 (0.18)

1.2.2 Biaxial Testing

As research continued, bladder tissue testing also included biaxial experiments since the bladder experiences both longitudinal and circumferential strain in-vivo during filling and voiding. Strain controlled biaxial testing devices includes two motors, orthogonal from each other, that apply a displacement on the sample in two orthogonal directions. The motors are connected to load cells that are used to obtain force measurements. A typical set up for biaxial testing can be seen in Figure 5.

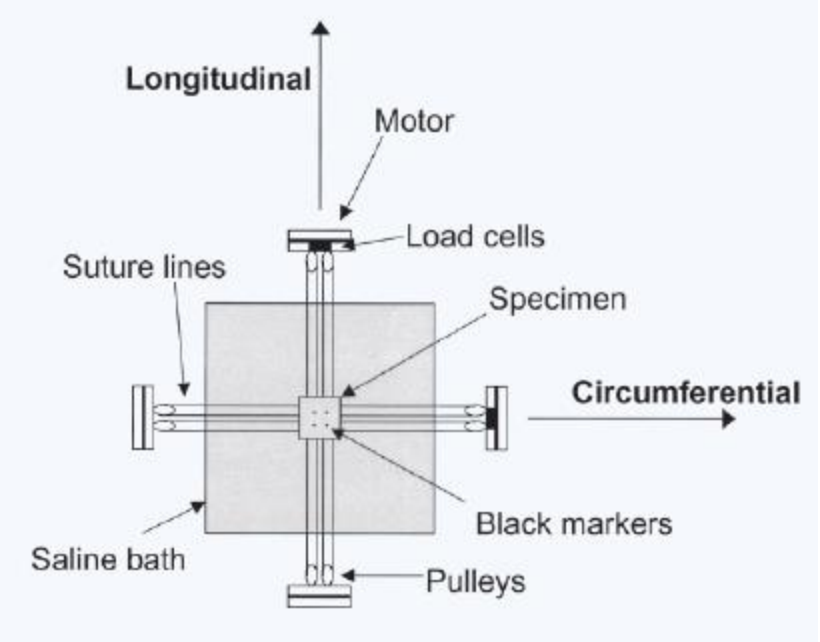

Figure 5 Typical biaxial testing setup (Reprinted from [11], with permission from Wolters Kluwer Health, Inc)

Research using biaxial testing from Gloeckner *et al.* [11] compared different ratios of biaxial stresses applied to a bladder sample. Gloeckner's work showed that a negative strain occurs in the circumferential direction at a load ratio of 1:0.5 where 100 kPa of stress was applied in the longitudinal direction and 50 kPa of stress was applied to the circumferential direction. This result could possibly be linked to the strong cross-coupling between axes [11].

1.2.3 Structure Function Relation

Moving forward, biaxial testing was coupled with advanced imaging techniques to re-evaluate the source of the bladder's large compliance [7]. In this study, Cheng *et al*. utilized a custom-built biaxial testing setup that could be used under a multiphoton microscope to directly measure layer-dependent collagen fiber recruitment in rat bladder samples. The samples were loaded, and their loading curves were related to the collagen fiber recruitment in the context of the

inner (luminal) lamina propria layer and the outer (abluminal) detrusor smooth muscle layer. The study divided the loading curves into three different sections: the toe, transition, and high stress regimes. The first important finding was that wall extensibility in the toe region was achievable by the bladder's undulations (folds known as the rugae shown in Figure 1). This finding can be seen in Figure 6 where the luminal side of the sample shows the undulations gradually flattening under increasing strain until the collagen fibers straightens out. On the abluminal side, undulated fibers also straighten with increasing strain.

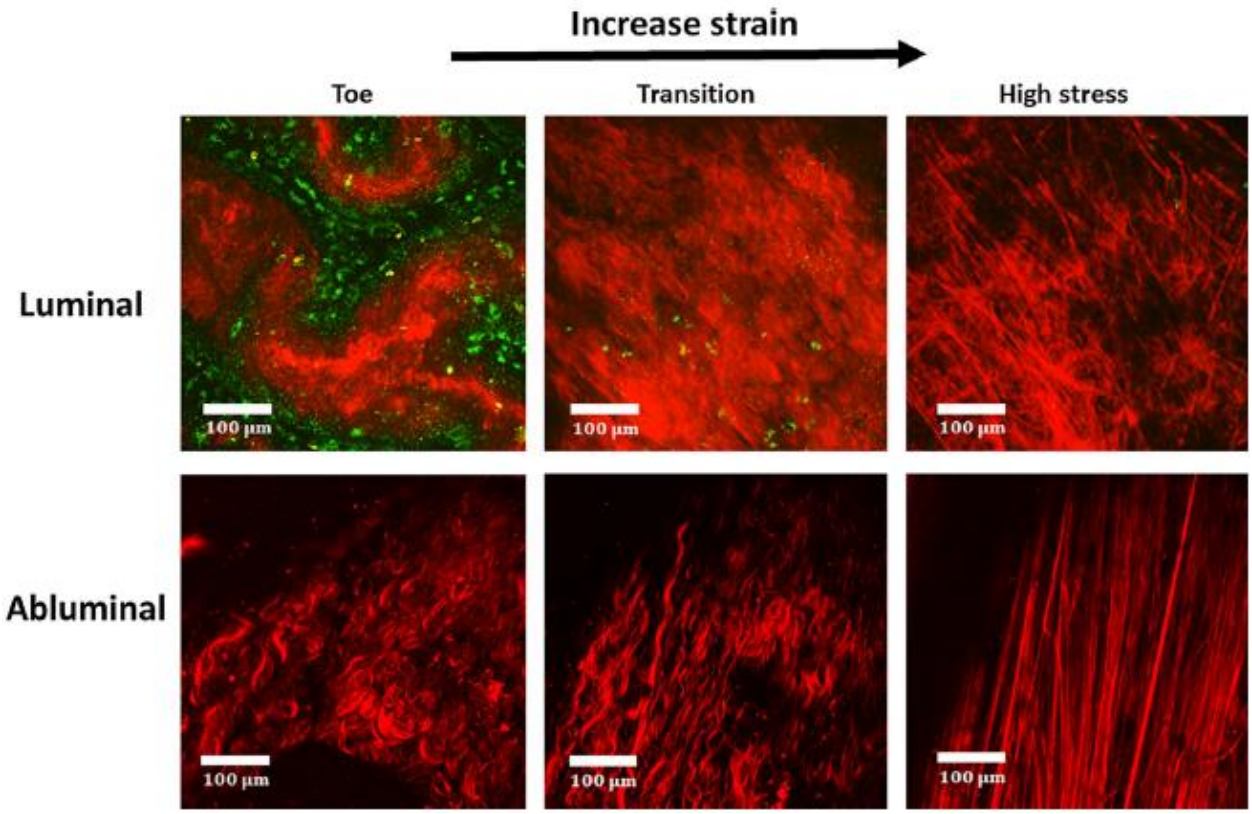

Figure 6 Projected stacks from multiphoton microscopy images showing an adult rat bladder sample. Luminal and abluminal images are shown at the toe, transition and high stress regimes (Reprinted from [7], with permission from Springer Nature)

The second finding showed that as age increases, wall extensibility can be lost by premature recruitment of the collagen in the abluminal side. This is shown in Figure 7, where the collagen fibers began to recruit (straighten out) at a much lower strain, causing the toe region to be shorter with the exception of an outlier from both the adult and aged samples.

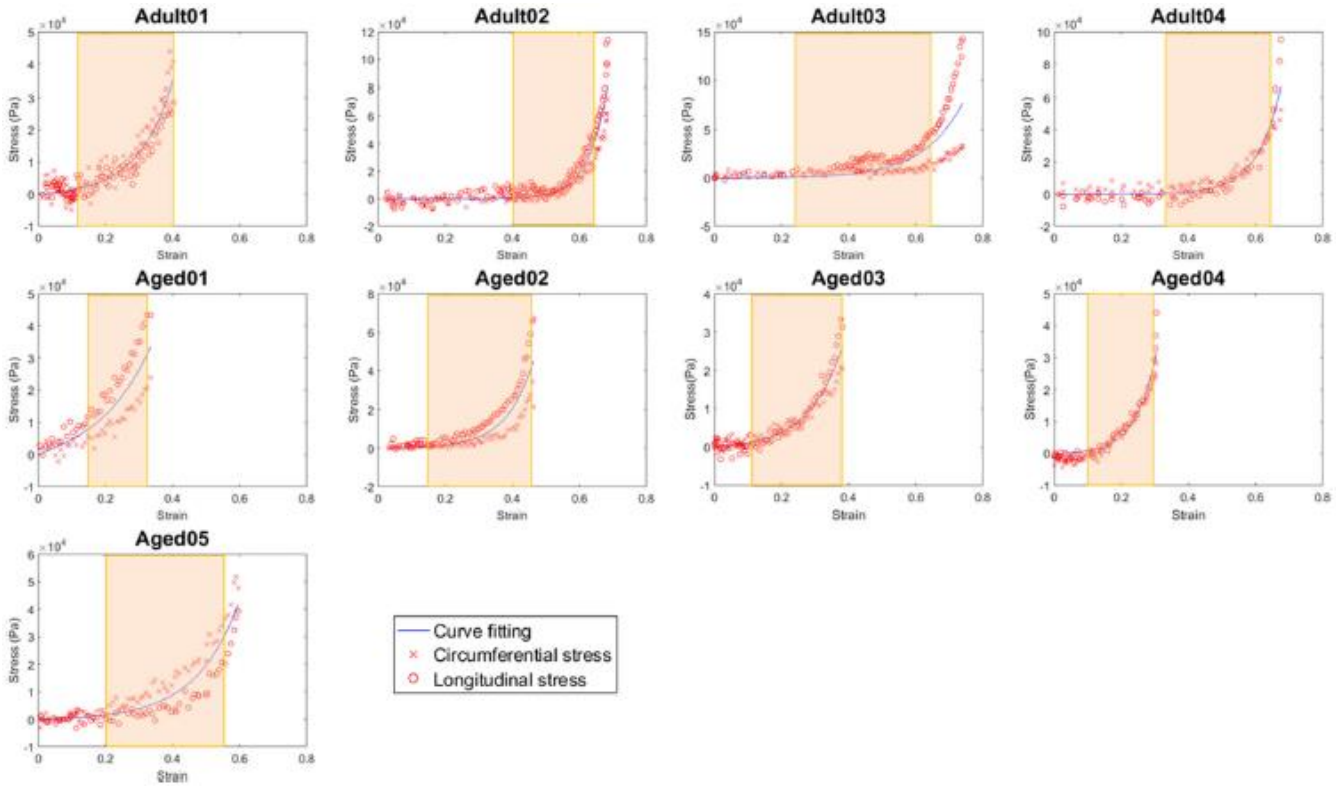

Figure 7 Mechanical loading curves for bladder tissue showing Cauchy stress as a function of strain. The highlighted colored rectangle represesnts the transition region between the toe and high stiffness regions (Reprinted from [7], with permission from Springer Nature)

This research allowed for a better understanding of the source of the large compliance by not only mechanically testing samples, but also by using advanced imaging to see what is occurring within the bladder wall during loading.

1.3 Bladder Functionality With Age

As mentioned in Section 1.1, a decrease in bladder compliance can negatively impact the functionality of the bladder. Figure 1 shows how compliance decreases with age. This decrease in bladder compliance is associated with an increase in bladder stiffness. One study by Chantereau *et al.* used uniaxial testing on six younger female bladders (mean age of 29) five, older female bladders (mean age of 70) and 13 older female bladders (mean age 83.5$\pm$ 12.5) along with other pelvic organs to determine the effect age has on mechanical properties obtained using uniaxial testing. No woman in the test population had any reconstructive surgery or clinically relevant pelvic organ prolapse. The results of this study can be seen in Figure 8 [9].

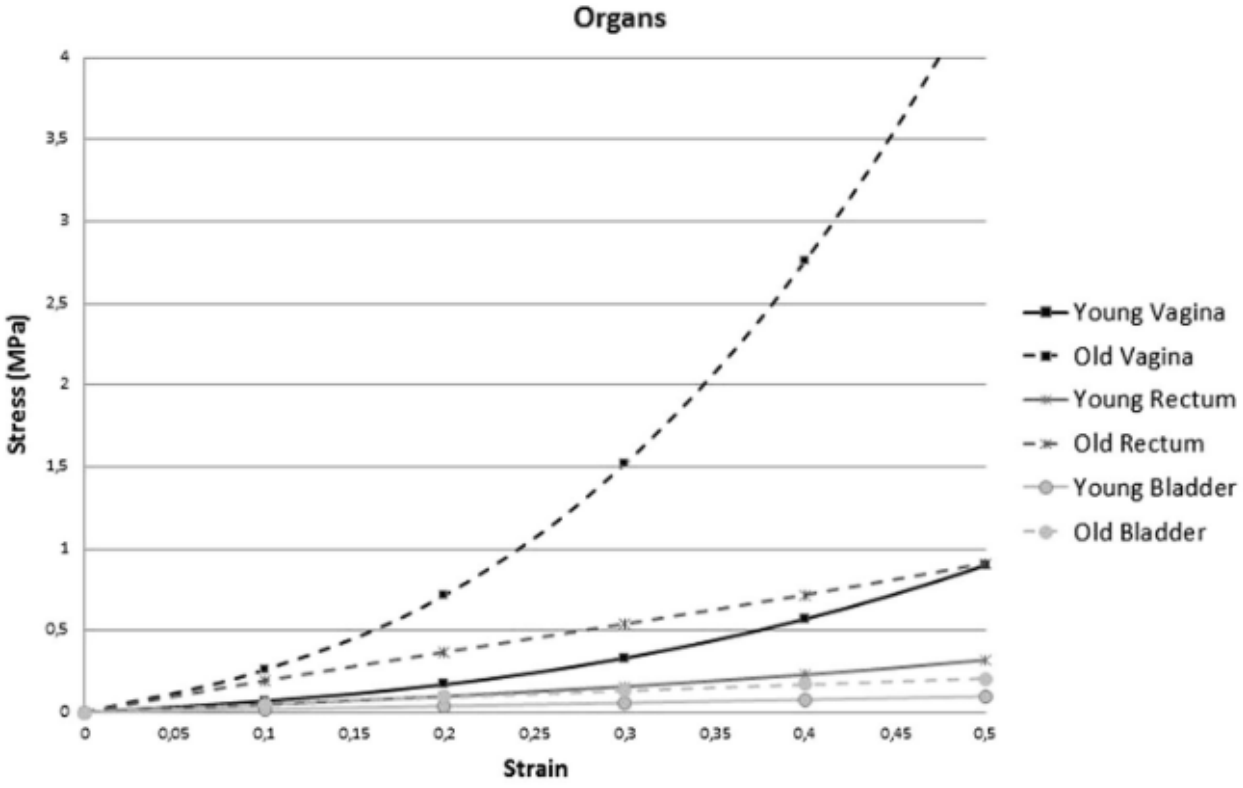

Figure 8 Median stress of female pelvic organs (Reprinted from [9], with permission from Springer Nature)

These results show that at every strain value, the younger bladder experiences a lower slope than the older bladder which leads to the conculsion that the older bladder has a higher stiffness value. This higher stiffness is consistent with the rest of the organs in the pelvis and the results from Figure 1.

1.4 Analysis of Heterogeneous Mechanical Properties

One assumption that is often made when studying a segment of the bladder is that the bladder wall properties are the same throughout the entire bladder. Studies like the one conducted by Chantereau *et al* used 24 total bladders but obtained a total of 54 samples for their uniaxial testing. This study followed harvesting protocols set by Rubod *et al* where the tissue was cut along the longitudinal axis of the vagina with an initial midline incision that served as the medial border [22]. This protocol does take into consideration orientation to be consistent with the other pelvic tissues harvested, but location in which the sample was harvested is not considered hence the study does not account for heterogeneity.

One recent study by Morales-Orcajo *et al* aimed to demonstrate that the mechanical properties and the microstructure of the urinary bladder wall are heterogeneous across the entire organ. They took twenty-eight urinary bladders from domestic pigs and took nine samples from each bladder from different locations as illustrated in Figure 6 [12].

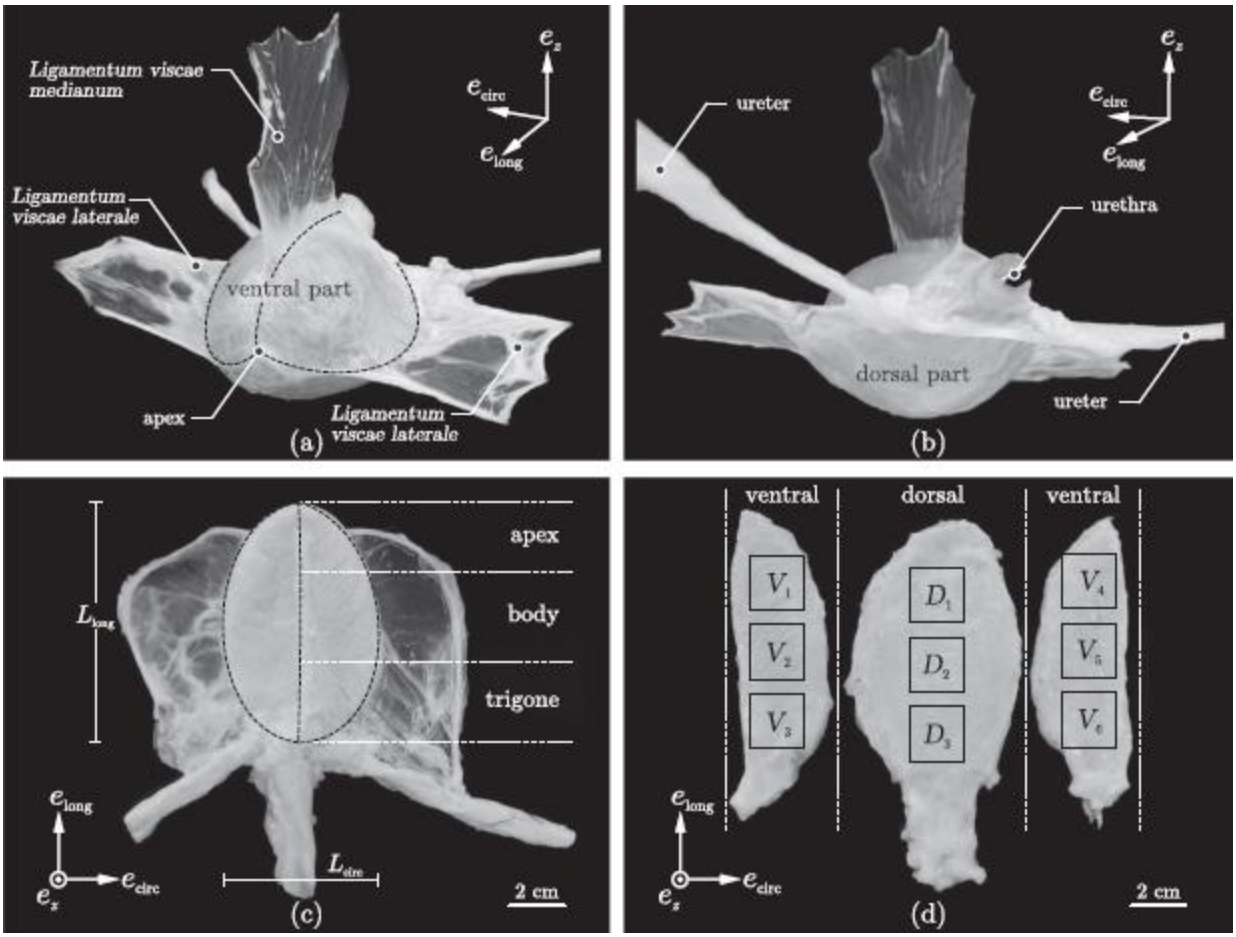

Figure 9 Porcine bladder anatomy and tissue sample dissection. (a) shows the anterior view of the bladder, (b) shows the posterior view and (c) shows the top view with the three divided regions: apex, body and trigone. (d) shows the sample locations from the outside view (Reprinted from [12], with permission from Elsevier)

These samples were then preconditioned through 12 successive stretch-controlled cycles from 1.3 to 1.4 and then cyclically stretched biaxially to analyze the Cauchy stress-stretch behavior. In the results of five of the tests, shown in Figure 10, the behavior of the sample is shown to be independent of its origins, but a noticeable difference in stress with resepct to strech can be seen, especially from samples cut from the trigone region. Furthermore, the sample was slightly stiffer in the longitudinal direction compared to the circumferential.

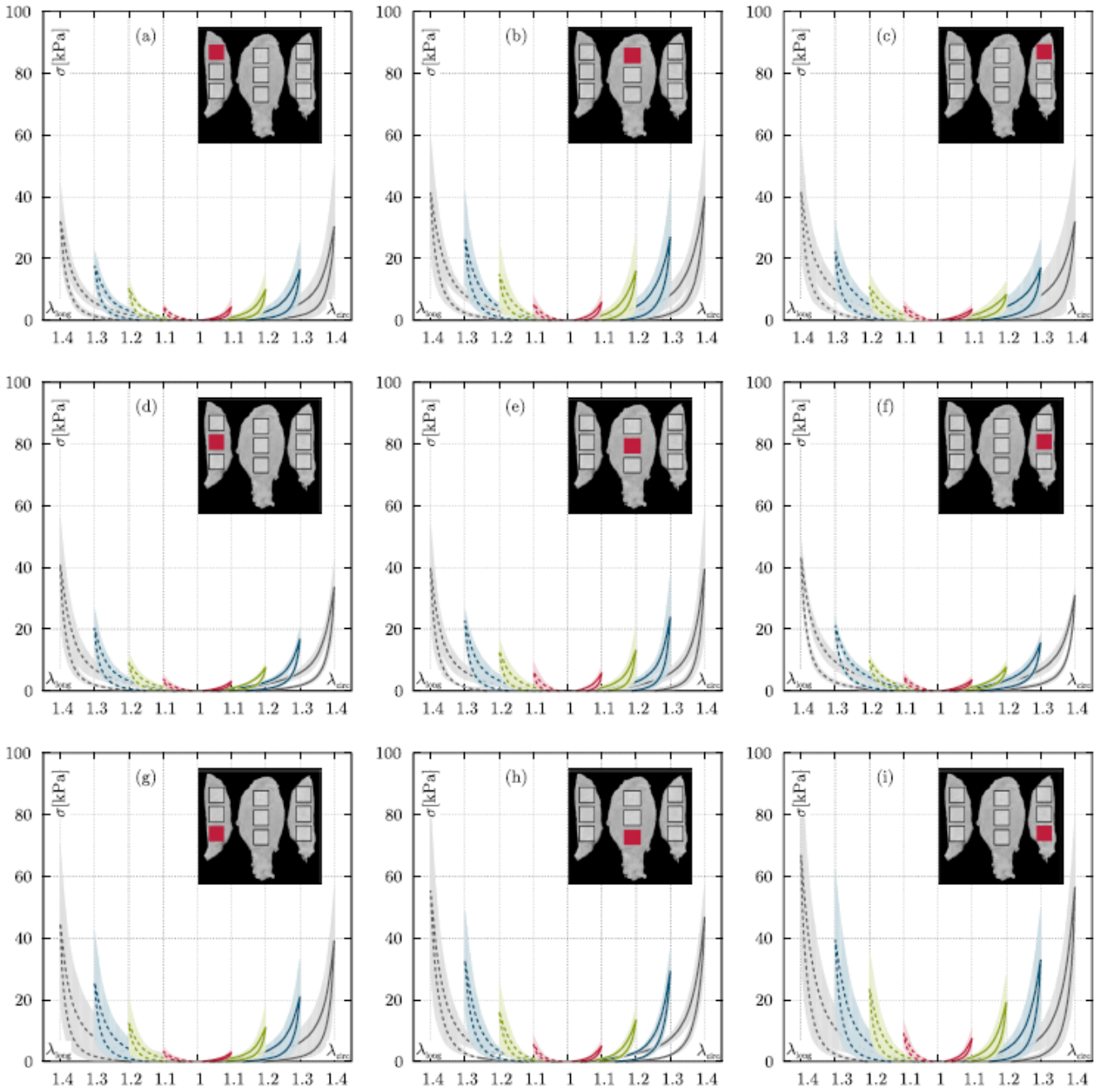

Figure 10 Location-dependent stress vs. stretch response of the urinary bladder wall. Red represents stretch of 1.1 before load is released, green represents stretch of 1.2 before load is releaased, blue represnets stretch of 1.3 before load is released and grey represents stretch of 1.4 before load is released. Dotted lines denote the longitudinal direction while the solid lines represent the circumferential direction. Shaded areas demonstrate the standard deviation (Reprinted from [12], with permission from Elsevier)

These results show that at stretches of 1 to 1.2, the sample is much stiffer. This is apparent when comparing the red and the green curves since the samples experience a lower change in stress compared to the blue and grey curves. The results also show that location of the bladder is sample effects the stress vs. stretch results and that the assumption of homogeneous mechanical properties can lead to incorrect modeling and discrepancies between research findings.

2.0 Technical Background

In this thesis, we leverage the use of powerful research tools to analyze the whole bladder. Using micro-CT, digital image correlation and the virtual field method, mechanical properties of the bladder can be determined noninvasively. In this chapter, these testing tools are presented and described to provide a fundamental background for the following chapters.

2.1 Micro-CT

Microscopic computed tomography (Micro-CT) is an advanced nondestructive imaging tool that stems from computed tomography scans (CT scans) that were introduced in the 1970s [13]. As advances in computing power and imaging came about, greater resolutions could be achieved leading to micro-CT being implemented in the laboratory settings as opposed to mostly clinical. These advances have allowed the study of samples of less than 1 nano liter in volume [14].

The system that was used in these experiments is the SKYSCAN 1272 from Bruker which is a high-resolution 3D X-Ray microscope that is based on micro-CT technology [15]. Most micro-CT scanners are similar in design, as shown in Figure 11, and include a tungsten-anode X-ray tube which is coupled to a high-resolution X-ray detector system. The X-ray detector system acquires projections of the sample at hundreds of angular positions. The sample is placed on a rotating stage at a position from the source typically between 7 and 18 cm referred to as source-to-object distance (SOD). The X-ray images are then acquired with the X-ray detector system which is typically at a

distance from the X-ray source of 20cm, also referred to as source-to detector distance (SDD) [14]. From here, post processing software is used to reconstruct the three dimensional image.

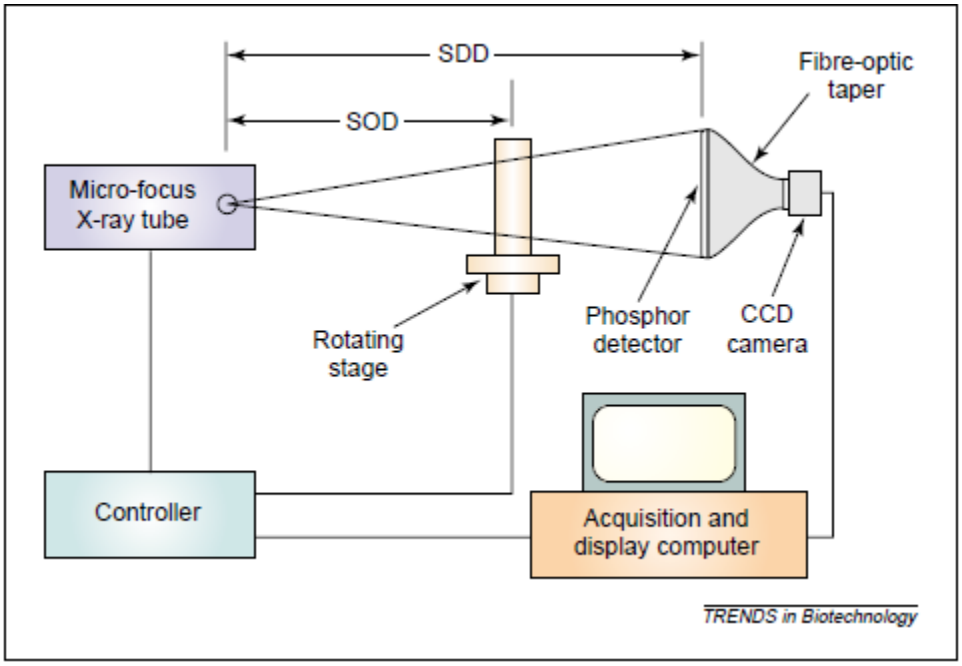

Figure 11 Diagram showing typical Micro-CT Scanner. SOD refers to source-to-object distance and SDD referes to source-to-detector distance. The Fibre-optic taper serves to reduce the image size. (Reprinted from [14], with permission from Elsevier)

2.2 Digital Image Correlation

Digital Image Correlation (DIC) refers to a three-step process in which images of an object are acquired while it deforms, those images are stored in a digital form and, finally postprocessing of the images is conducted to provide shape, deformation, and/or motion measurements [16]. DIC can be conducted in both 2D and 3D, but this research focuses solely on 3D-DIC. DIC is rooted in the discipline of image matching and employs algorithms that consider the geometry of the

deformation process. In using DIC on rat bladders, the resolution required to capture motion is much higher than larger samples because length changes are as low as 10^{-5} m/m [17].

For image matching to occur in DIC, the surface of the object must demonstrate certain properties. First, surface structures should be isotropic since any preference in a certain orientation limits the determination of motion vectors to orthogonal structures. Second, repeated textures lead to misregistration of structures and therefore a non-periodic surface texture is ideal. To meet these criterions, a random speckle pattern that adheres and deforms with the object is applied to the surface of the sample, examples shown in Figure 12, in order to lessen loss of correlation even when large translations and deformations occur [17].

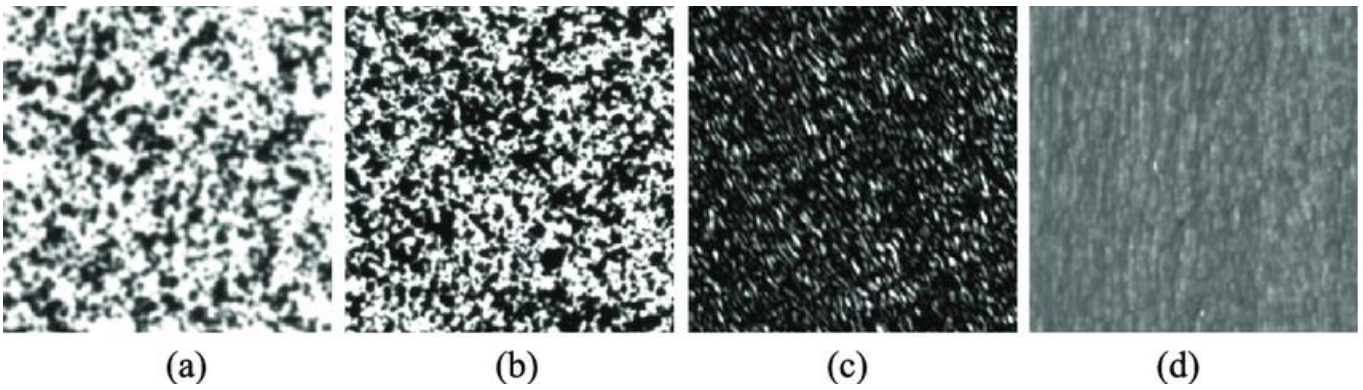

Figure 12 Examples of different speckling patterns. Patterns (a) and (b) show painted patterns, (c) shows laser pattern and (d) shows textur pattern which is made by spraying black/white pains, illuminating the surface with a laser and deriving from the samples natural texture [18]

After speckling, images are obtained using two stereo cameras which record data necessary to generate 3D images by positioning the cameras at different angles (in this work one at 15 degrees and the other at -15 degrees). With the set of images, the DIC algorithm, in this case implemented in VIC-3D software by Correlated Solutions, creates a projection of the displacement field of the object for each image. This is done by assigning an X, Y and Z position for each data point created

by the speckles and then projecting the data points. This projection is based on the area of interest chosen by the user and is output as a topographic map of the sample as shown in Figure 13.

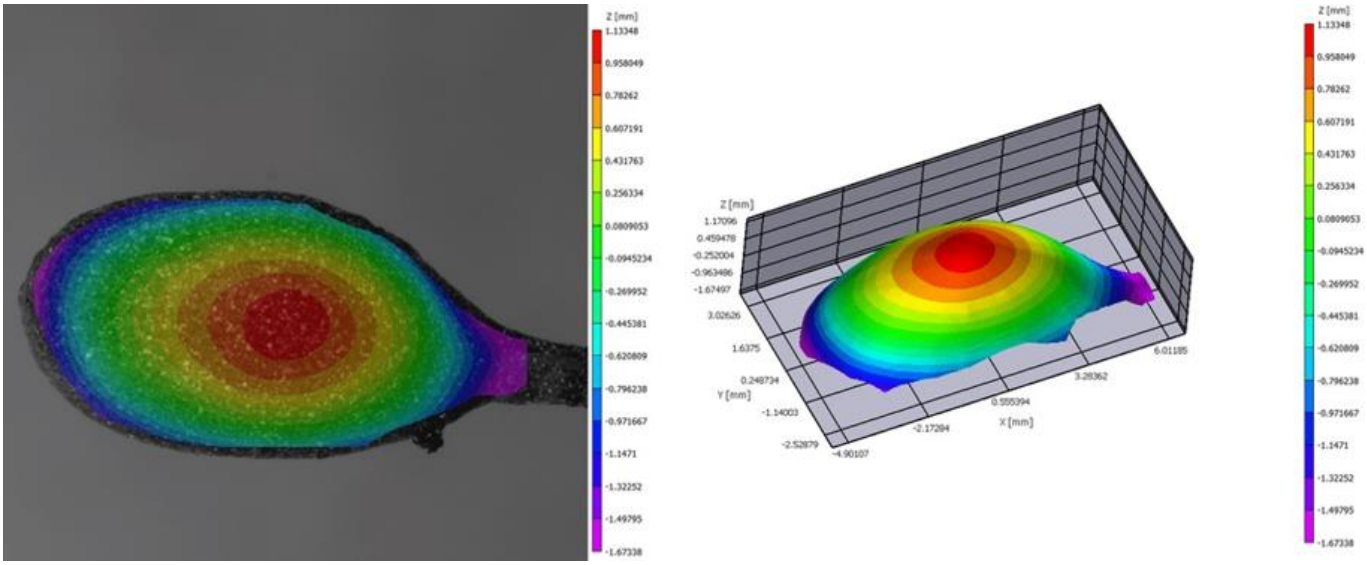

Figure 13 Projection of Z-position for a bladder. (a) Projection superimposed on image of bladder (b) 3D-reconstruction of the bladder projection. Images generated from the data obtained from thesis research.

Finally, with these projections for numerous loading levels, an algorithm is used to calculate the strain. In short, the algorithm takes the data points from the projection and creates a grid of points that contain and X, Y and Z positions as well as a U, V and W displacement vector shown in Figure 14(a). From here, each point of the grid is considered separately, and a local mesh of triangles is developed with the adjacent points shown in Figure 14(b). Next, each triangle is analyzed separately for all loading levels shown in Figure 14(c) and the strain tensor shown in Figure 14(e) is computed for each triangle. These results are interpolated to provide a strain for the data point Figure 14(f). This process is repeated for each data point in the grid. Any rigid motion is removed since each deformed triangle produced has a reference triangle that can be mapped back to Figure 14(d) [19].

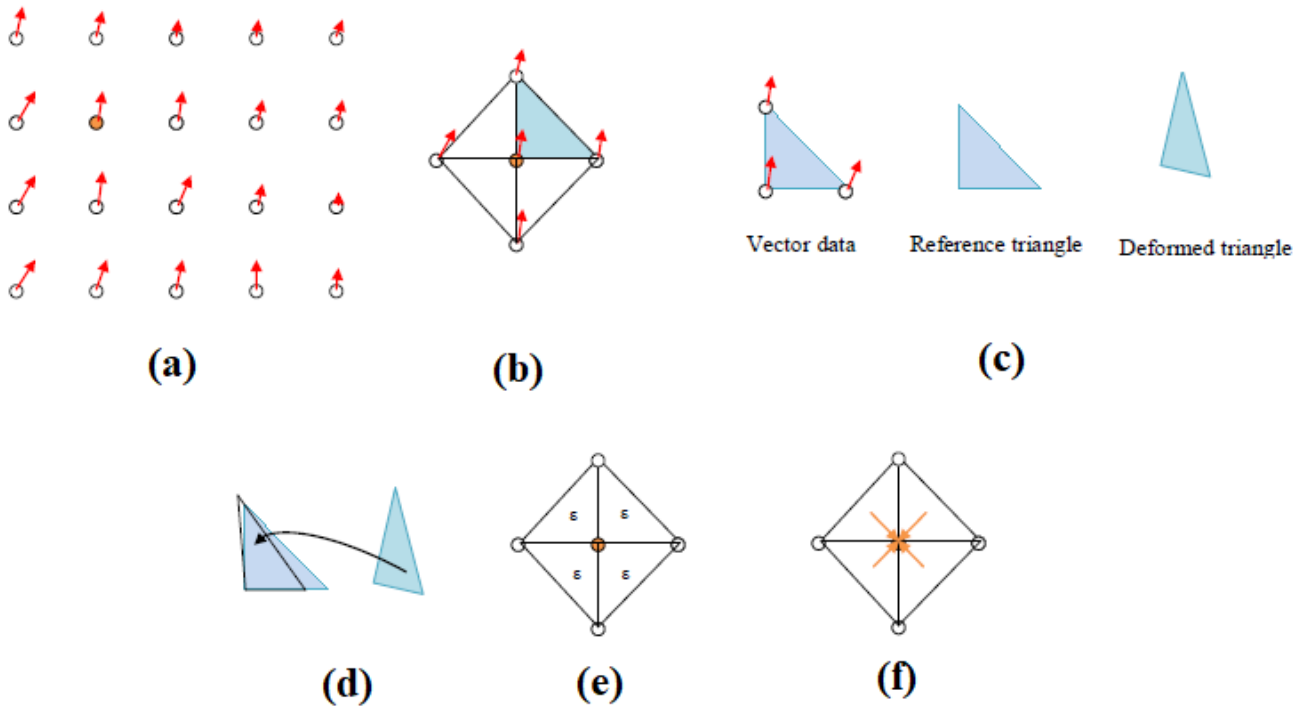

Figure 14 DIC strain calculation process. (a) Grid of data points and displacement vectors with one highlighted orange circle to be focused on. (b) Local mesh of triangles created from data point being analyzed. (c) One triangle from mesh shown with its displacement vectors and the corresponding reference and deformed triangle produced. (d) Diagram showing deformed triangle being mapped back to reference triangle to remove rigid motion. (e) Strain calculated for each triangle. (f) Strain tensors interprolated to calculate a strain value for the data point. [19]

2.3 Virtual Field Method

The virtual field method will be used in this work to obtain maps of the material stiffness over the bladder surface noninvasively from knowledge of the wall thickness and strain fields. The virtual field method is a modeling approach that quantifies material properties [24]. This method

takes full field deformation measurements along with wall thickness values that, in this thesis, are obtained with digital image correlation and micro-CT to calculate stiffness values.

This method has been used in the past to access material properties for ascending thoracic aortic aneurysms using preoperative CT-Scans. The stiffness values for aneurysms can potentially be used to provide a more accurate risk of rupture. The researchers used the scans and placed a mesh and nodes over them in order to determine local strain distributions. Using this strain along with tension values, they were able to solve for local extensional stiffness at every position in the mesh as shown in Figure 15 for the three patients examined. The higher stiffness areas show where the ascending aorta is believed to be most likely to rupture [20]. It should be noted that tension, not stress, was calculated in this work as wall thickness was not known.

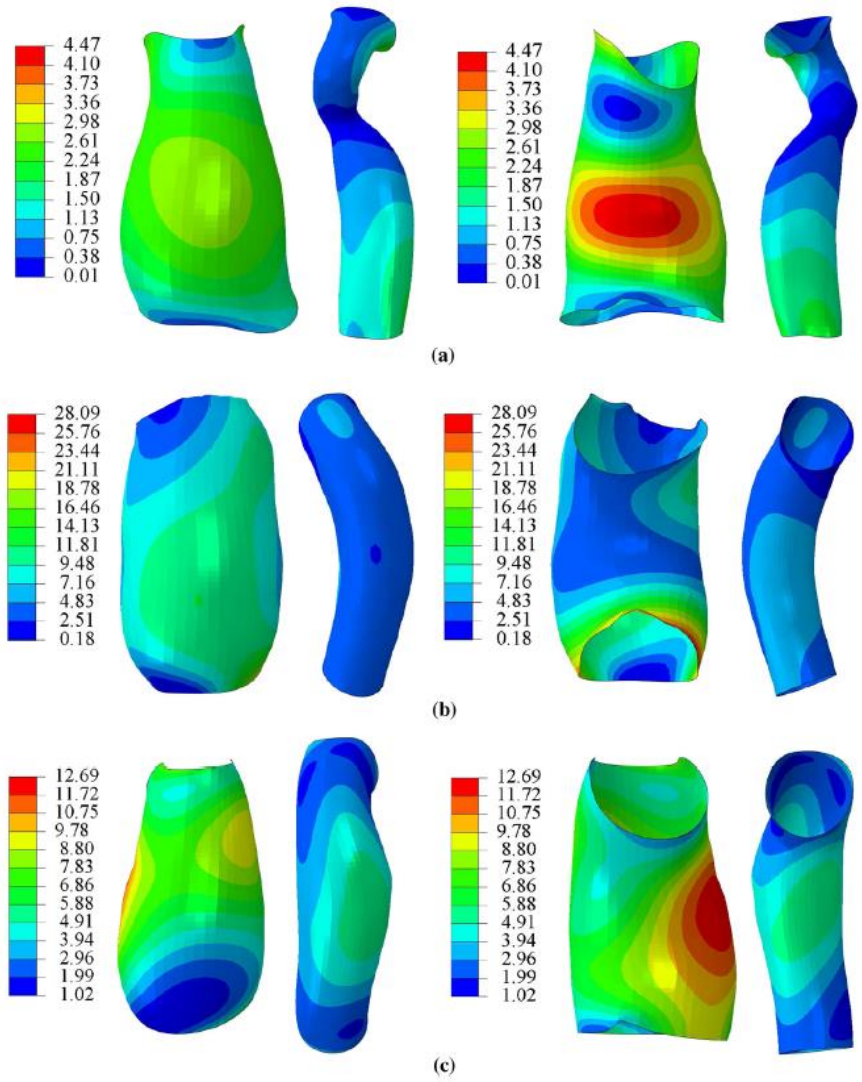

Figure 15 Distribution of local extensional stiffness (MPa mm) in ascending and descending aortas for Patient 1(a), Patient 2(b) and Patient 3(c). Left and right columns show frontal and distal views respectively (Reprinted from [20], with permission from Springer Nature)

3.0 Methodology

In this Chapter, the specific methods in which the results were obtained for this thesis are presented. The methods for testing rat bladders required some modifications to the micro-CT and DIC protocols to allow for soft tissue to be properly analyzed. The large deformation the bladder experiences and requirement to maintain the sample in an environment where it will not dry out, made testing difficult. The virtual field method was used in collaboration from Dr. Stephane Avril's group from Ecole des Mines de Saint-Etienne. Their work on the virtual field method allowed us to obtain an estimate of the shear modulus throughout the sample for the first time.

3.1 Overview of The Study

The steps in the protocol used in this thesis are conducted in the order shown below in Figure 16. Briefly, the bladder is harvested and prepared for experimentation with the insertion of a luer-lock syringe as shown in Figure 16(a). The bladder is then imaged at two pressure levels of 7 mmHg and 35 mmHg using the micro-CT so that shape and wall thickness color maps can be obtained as shown in Figure 16(b). Following micro-CT, the bladder is then speckled as shown in Figure 16(c) and analyzed using DIC to obtain a strain-field color map similar to the one shown in Figure 16(d). Finally, shear modulus results are obtained using the virtual field method with the wall thickness data and strain data similar to the data shown in Figure 16(e).

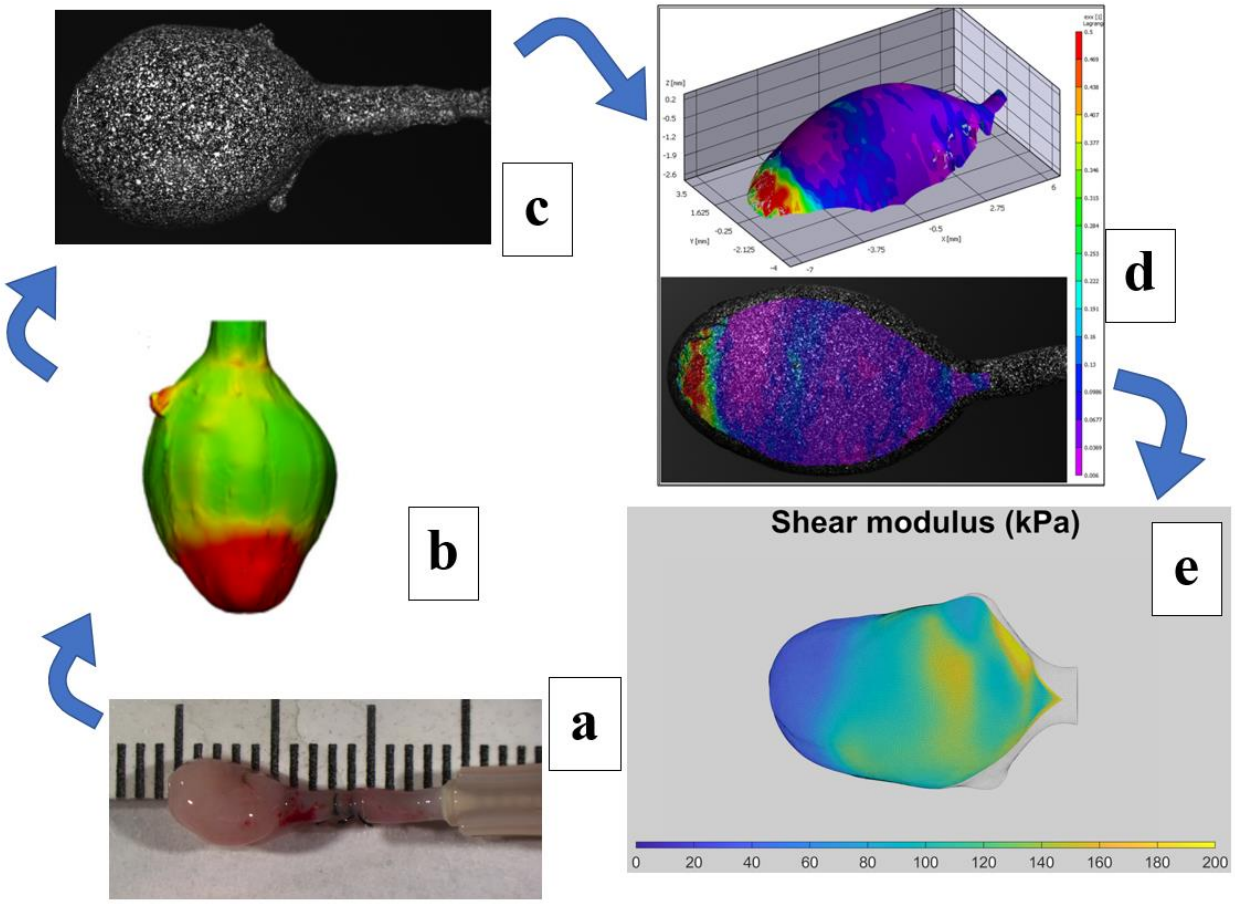

Figure 16 Diagram illustrating overview of studies conducted. (a) Image of bladder immediately after harvesting. (b) Wall thickness color maps obtained from micro-CT imaging. (c) Speckled bladder. (d) Strain map obtained using DIC for E_{xx}. (e) Shear modulus map obtaineed on portion of the bladder using virtual field method.

3.2 Methods: Sample Preparation

The samples used in this study are from young female rats from control and treated groups between the ages of 3 to 4 months. The bladders were harvested same day the experiments were ran. When harvesting, the ureters are and urethra are cut and the ureters are cauterized to seal them for experiments. Control bladders were used in which no medication was given to the rats prior to

harvesting the bladder. Treated rats were given hypoxanthine for three weeks prior to harvesting. A luer-lock adapted needle was inserted in the urethra and tied using sutures to allow inflation of the bladder for the studies. An image of the harvested bladder attached to the needle can be seen in Figure 17 below. The bladder was then submerged in a solution of Hank's buffer salt solution (HBSS), EDTA (chemical binder) nifedipine (voltage calcium channel blocker) and Thapsigargin (SERCA pump inhibitor to prevent reloading of intracellular calcium stores) to inhibit smooth muscle cell contractions which may affect data collection. The contents of this solution are outlined in Table 2.

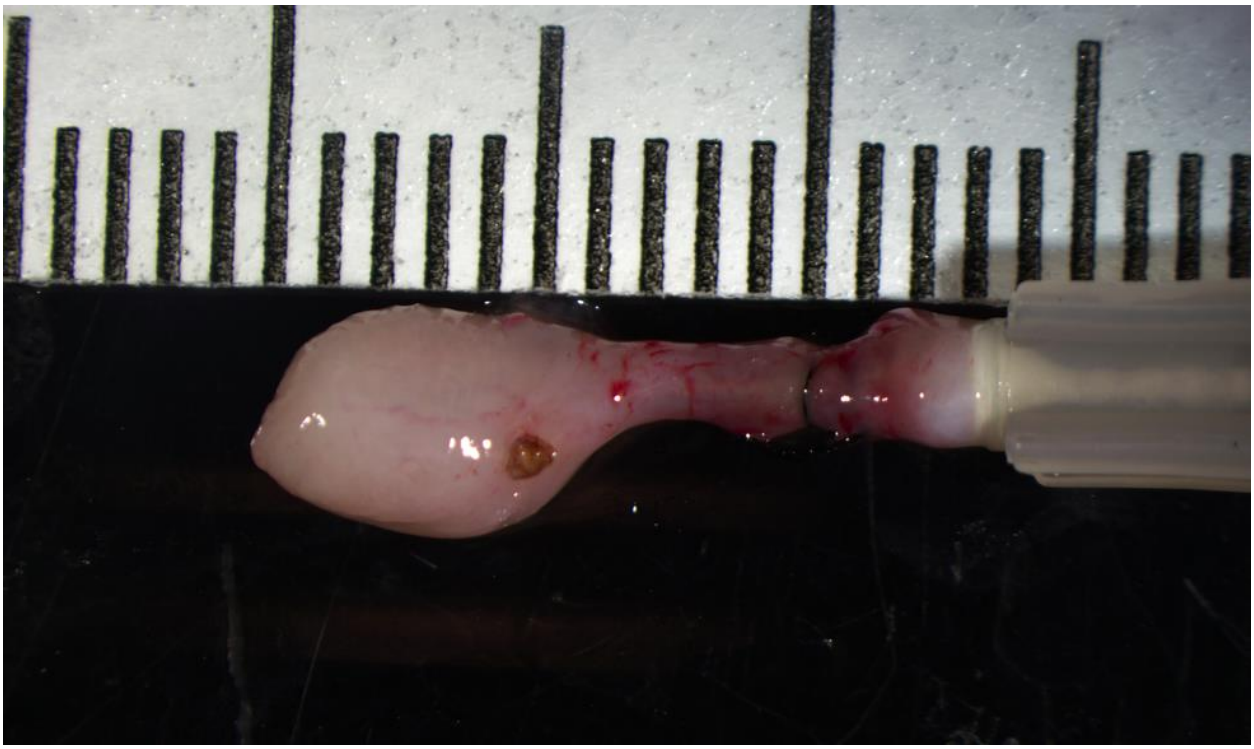

Figure 17 Prepared harvested bladder with luer-lock adapted needle

Table 2 Contents of solution for smooth muscle cell contraction inhibiting. Solution is at pH 7.4 and osmolarity 310 mOsm/L (Reprinted from [14], with permission from Springer Nature)

Substance	Quantity (mM) @ pH 7.4 and 310 mOsm/L
NaCl	138
KCL	5.00
KH2PO4	0.30
NaHCO3	4.00
MgCl2	1.00
HEPES	10.0
Glucose	5.60
EDTA	0.5
Nifedipine	0.005
Thapsigargin	0.001

3.3 Methods: Micro-CT Studies

To obtain the shape and wall thickness of the bladder, two micro-CT scans were conducted on the bladder, one at a low pressure of 7 mmHg and one at a higher pressure of 35 mmHg. 7 mmHg was chosen to allow the bladder to be slightly inflated. 35 mmHg was chosen since it was one increment below the maximum inflation in this study. Wall thickness is analyzed over the entire bladder for both pressures and a 3D model is created. Scanning soft tissue, such as arteries and bladders, presents challenges that need to be circumvented to insure proper imaging and preservation of the sample.

3.3.1 Preconditioning

Before the sample can be tested, it is imaged under a microscope to record the physical appearance of the sample before testing, Figure 17. From there, any remaining liquid in the bladder post-harvest is extracted as moisture will negatively affect micro-CT images since water droplets will result in artifacts on the bladder. Next, the bladder is preconditioned by inflating it to a pressure of 35mmHg and deflating to a pressure of 5 mmHg, for three cycles using the programmable syringe pump BS-8000 from Braintree Scientific shown in Figure 18.

Figure 18 Braintree Scientific programmable syring pump BS-8000 used in bladder inflation

3.3.2 Preparation of Sample

To obtain useful micro-CT data, the bladder must not move during scanning to avoid motion artifacts. It must also be free of any moisture which can be indistinguishable from the tissue. This presents a challenge as the bladder dehydration could cause the mechanical properties to be affected. The bladder may also wrinkle due to the shrinkage caused by the sample drying out. In our experiments, the voided bladder was first pressurized with air to 5mmHg. The syringe was then sealed using a needleless injection site male luer-lock adapter #80147 from Qosina to prevent leakage that would cause motion during the scan. The bladder was then placed in a small test-tube which has been modified to allow the bladder to hang freely during scanning. A paper saturated with water is placed in the test tube to serve as a source of humidity to keep the bladder

hydrated during scanning. An image of the micro-CT testing device can be seen in Figure 19 below and the inflation system used can be seen in Figure 20. Finally, the test-tube is sealed further with parafilm. After the low-pressure scan, the external surface of the bladder was hydrated in deionized water for 15-minutes and then inflated to 35mmHg for the next scan.

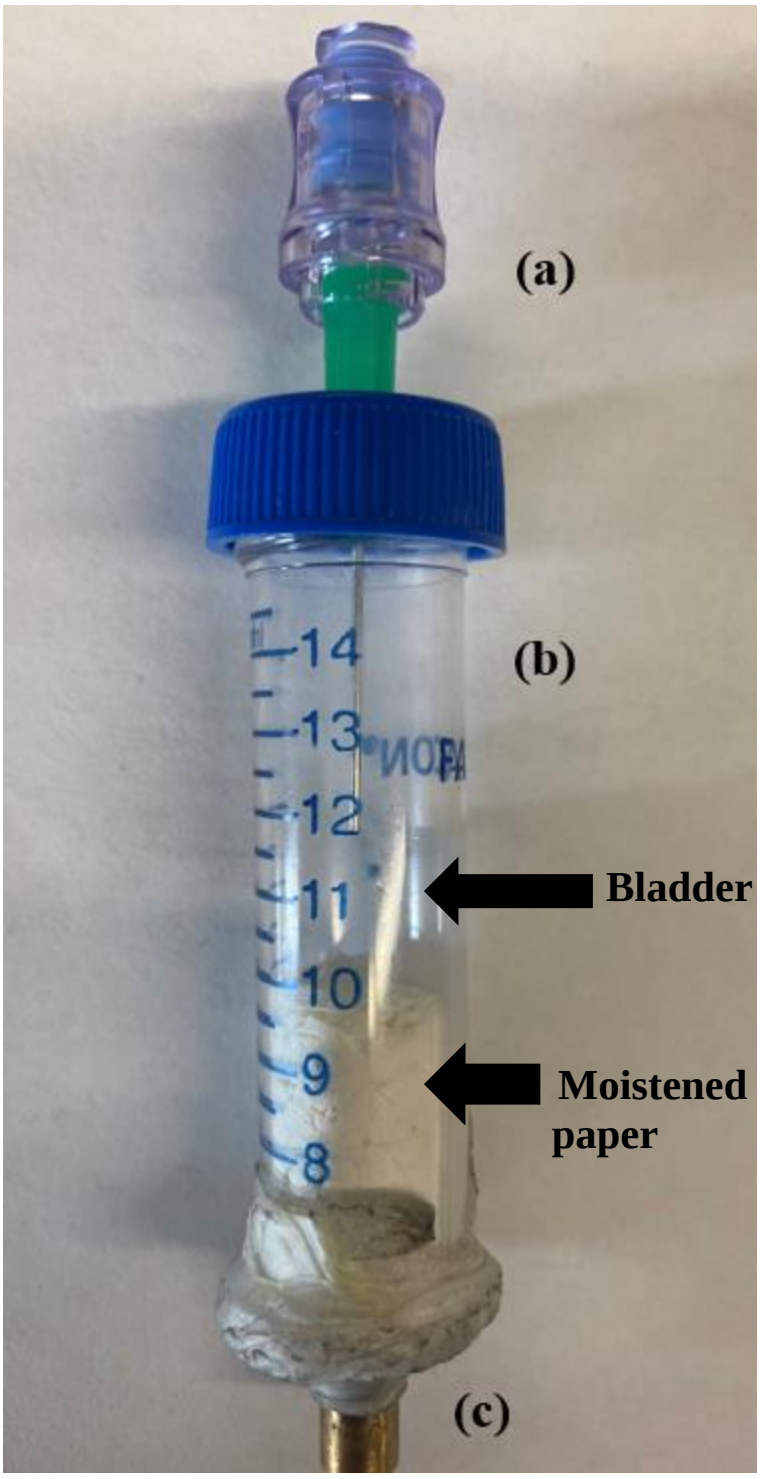

Figure 19 Micro-CT bladder testing device. (a) Needleles injection site adapter from Qosina attached to the syringe needle where the bladder is placed. (b) Modified test tube used with wet paper inside for humidity control. (c) Location where the device is connected to the micro-CT device.

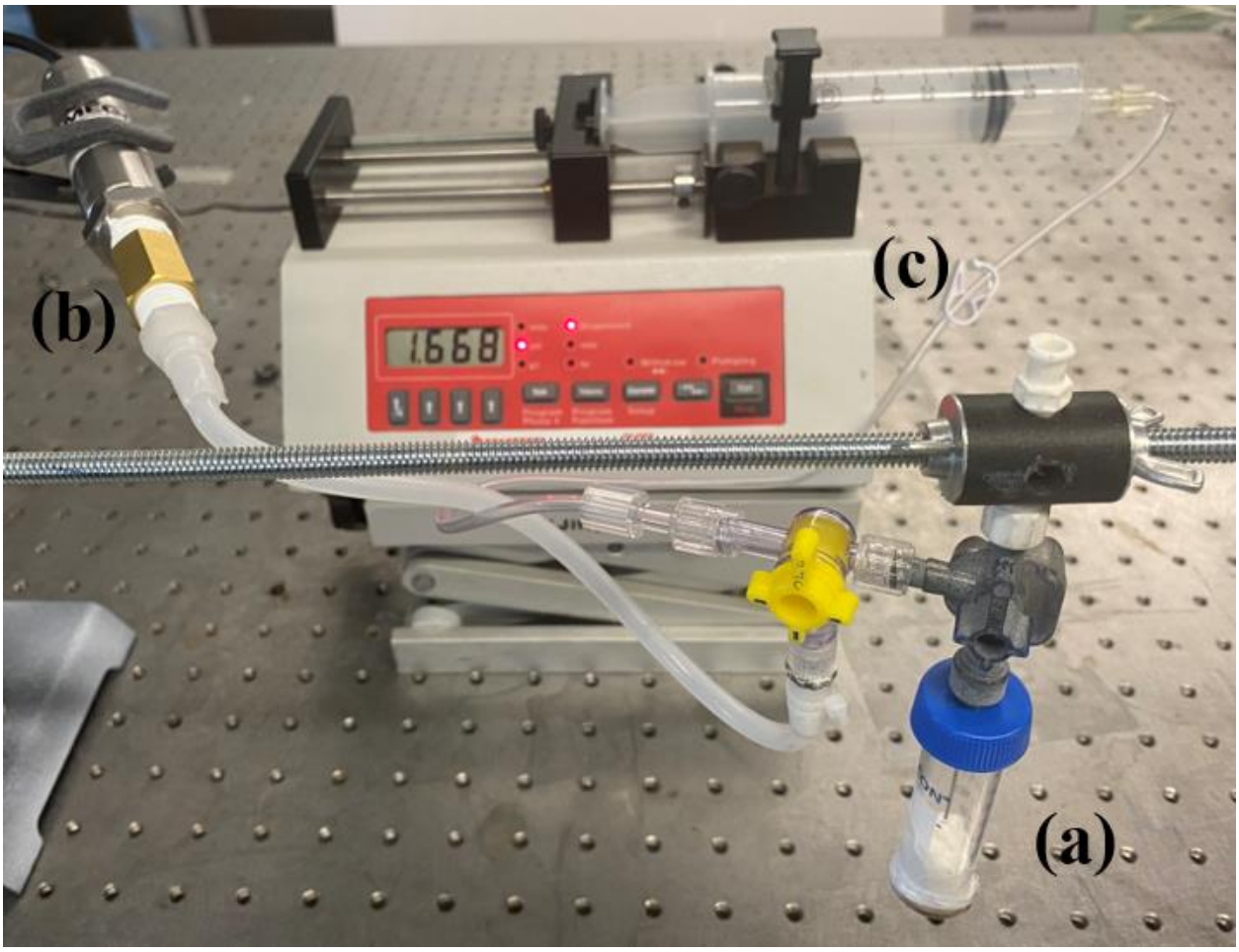

Figure 20 Inflation system. (a) Micro-CT testing device mounted on system, (b) Pressure transducer and (c) Syringe pump

3.3.3 Analysis

During scanning, the micro-CT system rotates the bladder 180 degrees and takes images every 0.3 degrees. These images are then used to create a 3D reconstruction of the bladder that can be used to analyze its geometry. With the images obtained from the micro-CT, several hundred slices are created depending on the length of the bladder. These slices show sections of the bladder along the length of the sample. The slices are then edited using ScanIP, a 3D-image processing and modeling software by Synopsys. In ScanIP, glares, rings and other unwanted artifacts are

removed from the slices and the slices can be reconstructed to create a model in STL format. This STL file is then uploaded to 3-Matic software by Materialise where the geometry of the bladder can be analyzed and a model displaying localized wall thickness can be created. Finally, to obtain a better view of the changes in wall thickness, the bladder model was divided into three segments based on results from micro-CT analysis, as shown in Figure 21. These sections were chosen to better understand and visualize the change in wall thickness. Specifically, this enabled different thickness length scales for the different regions The first section included the urethra and was cut right above the ureters and is referred to as the urethra section. The second section was the middle section of the bladder which included the ureters and bladder up to the area before the wall thickness begins to increase. Finally, the third section was the dome section of the bladder, which is where the wall thickness is greatest. The dome section, the region opposite to the urethra, is the last to expand and hence the wall thickness thins there last.

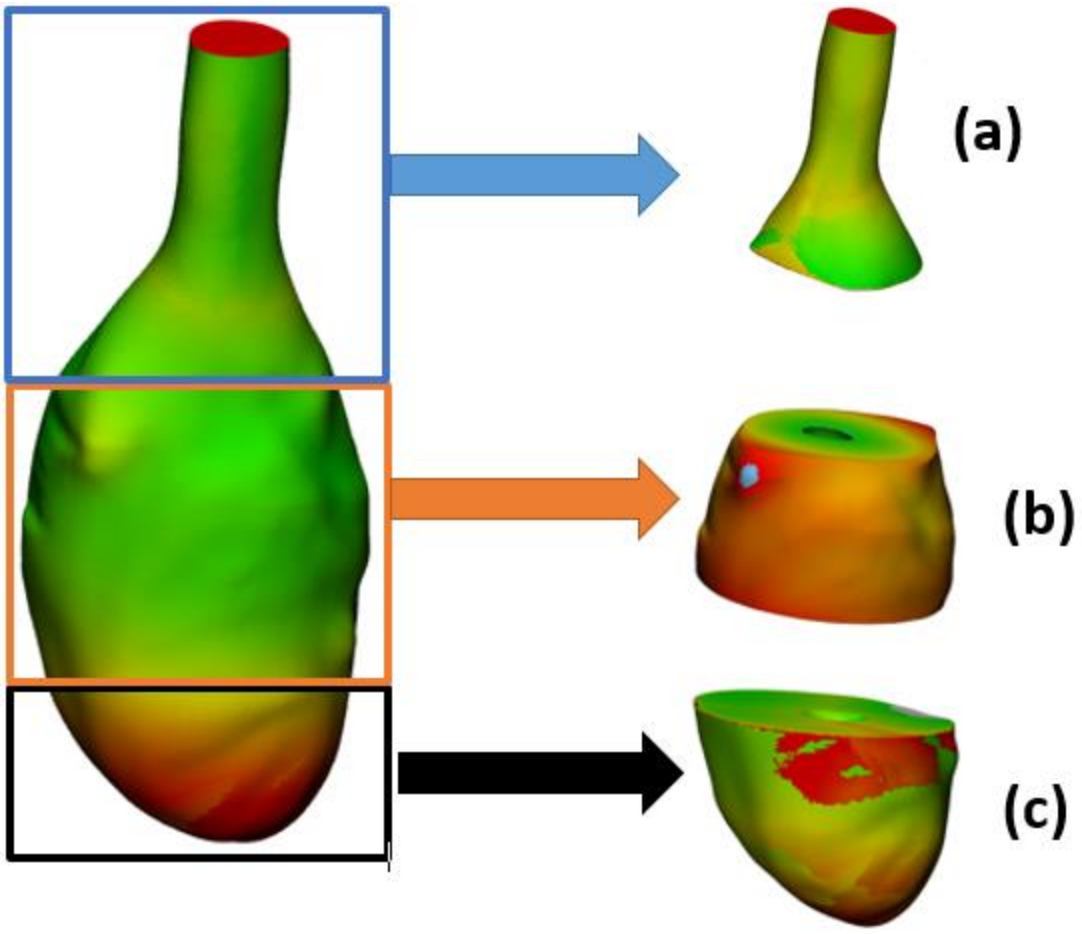

Figure 21 Sectioning of bladder reconstruction for better observation of local wall thickness change. (a) Urethra section (b) Middle section and (c) Dome section

3.4 Digital Image Correlation Studies

DIC allows for local strain values to be obtained across the entire region of imaging. Careful setup and preparation were followed to ensure that valuable and repeatable data is obtained without having to sacrifice many rats. Aside from ensuring that the bladder is properly handled, the system itself must be properly calibrated and adjusted to effectively analyze the sample.

3.4.1 Preparation of Sample

After micro-CT images are taken, the bladder is placed back in its original solution, outlined in Section 3.2, to rehydrate. After it has been rehydrated for a minimum of 15 minutes, the bladder was blotted to remove any excess moisture and the surface was allowed to partially dry. This was necessary because excess surface moisture prevents the bladder from being properly speckled and causes the ink to run and cause streaks. The Paasche H-set airbrush was used to speckle a fine random pattern of black and white India ink on the surface of the bladder, as shown in Figure 22, which provides an adequate contrast for DIC imaging. This speckling pattern adheres to the bladder and deforms along with the bladder. The ink speckles are allowed to dry for 20 minutes to prevent any ink run off.

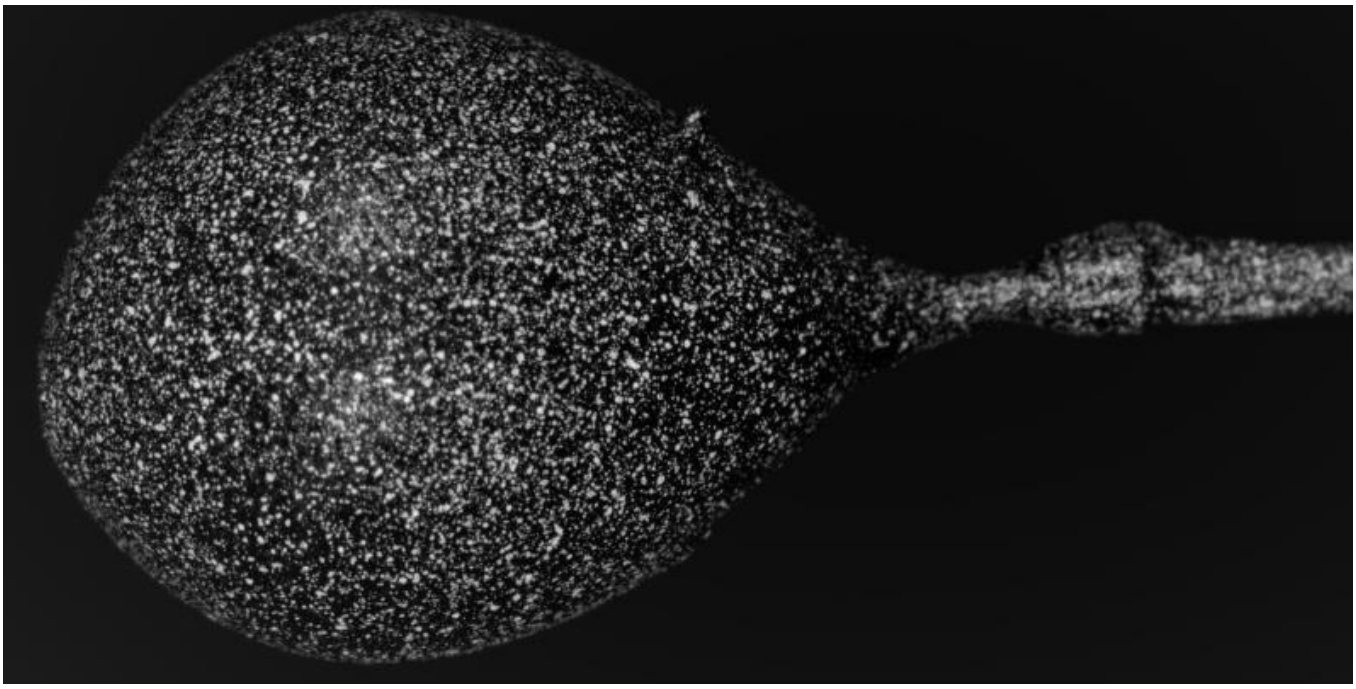

Figure 22 Speckled bladder

After the ink has been allowed to dry, the bladder surface is again hydrated briefly with deionized water, and excess liquid is carefully removed to prevent ink bleeding. From here any adjustments to speckling are performed to make sure the speckling provides a proper contrast and density.

3.4.2 Mounting and Test Setup

After the bladder has been prepared for imaging, it is mounted onto a custom-made setup, shown in Figure 23, which allows unobstructed imaging to occur. The bladder is allowed to hang freely in front of the cameras while it is connected to both a pressure transducer to keep track of pressure readings and an automatic syringe pump that inflates it. The DIC system is equipped with two 2.3-megapixel cameras from Correlated Solutions and Schneider Xenoplan 2.8/50mm compact lenses fitted with 20 mm extension tubes and polarizing lens caps. Two cameras are oriented at approximately 15 and -15 degrees to create an overlap in imaging and provide data from 2 orientations so a 3D reconstruction can be performed. Polarizing lens caps are used to reduce glare on the sample which occurs due to its surface moisture and the reflection from the LEDs used to illuminate the sample. The LEDs are also fitted with polarizing film to further reduce glare.

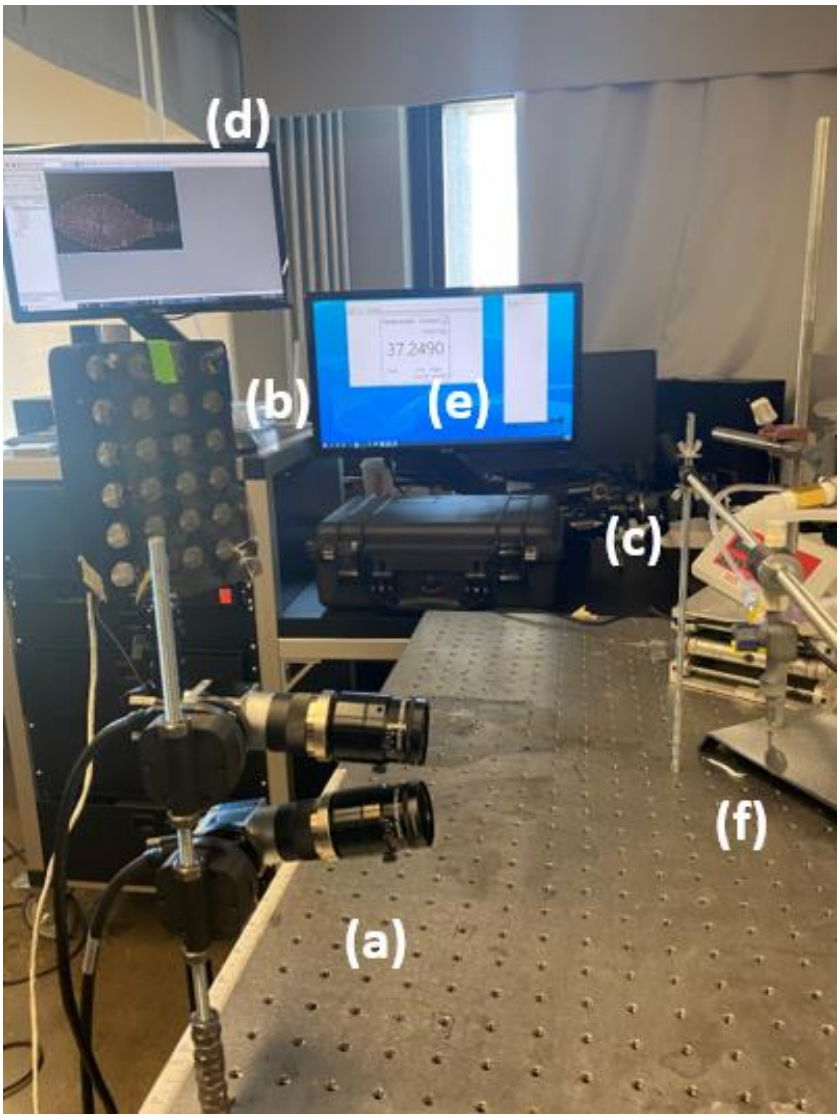

Figure 23 DIC Testing setup. (a) Stereo cameras, (b) LED lights fitted with polarizing film, (c) syring pump, (d) VIC-3D output (e) pressure transducer readings and (f) mounted bladder.

After the cameras are focused allowing the speckle pattern to be clear, calibration images are taken using a 1.78 mm spaced glass calibration grid from Correlated solution at the same location the bladder is mounted. The calibration grid is shown in Figure 24. These calibration images are used to provide positional information of the cameras that is needed for the VIC-3D algorithm to properly examine the bladders movements. Improper calibration leads to projection

errors that can lead to unreliable data. If this happens, calibration images can be retaken to provide a better calibration score as long as the cameras have not been moved or adjusted after the bladder data was obtained.

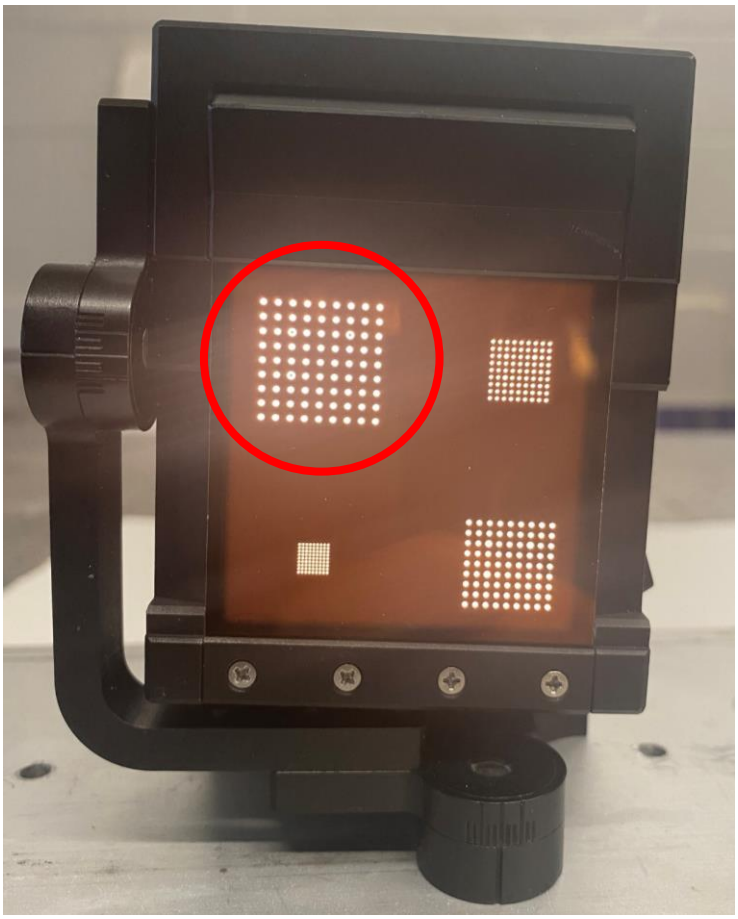

Figure 24 4-in-1 Calibration grid from Correlated Solutions with backlit fixture to illuminate grid. 1.78 mm grid used in tests (circled).

3.4.3 Inflation and Imaging

All inflation that occurs in this study is done with air from a syringe. As stated in Section 3.3.1, the inflation is performed with the programmable syringe pump BS-8000 from Braintree scientific. The flow rate can be adjusted depending on the size of the bladder to ensure a steady flow of air into the bladder. To monitor and record the pressure of the bladder, the PX409-060GUSBH pressure transducer from Omega Engineering is used. Pressure readings are taken of the bladder in increments of 5mmHg starting from 5mmHg up to 40mmHg. At each pressure increment, the pressure is allowed to stabilize and make sure that there are no potential leaks in the system. At each pressure increment, an image is taken of the bladder using the VIC-Snap software from Correlated Solutions. These images are the data that will be used to calculate the projections and ultimately the strain fields.

3.4.4 Data Analysis

After the calibration images and speckled bladder images are obtained, the raw data can be imported into VIC-3D. Within VIC-3D, the calibration images are analyzed to make sure the error between the two cameras is sufficiently low. Each calibration image is compared to the same image from the second camera to make sure all points on the calibration grids are mapped back. If any points are not mapped back, the calibration score is affected. As previously noted, if the error is sufficiently large, calibration images must be retaken, to ensure accurate camera positioning information is acquired.

When calibration is complete, the speckled images (images of the bladder at each pressure increment) can be uploaded. An area of interest for analysis is chosen and starting points can be

manually selected. As for the analysis of the calibration images, the algorithms used within VIC-3D searches for matching speckles between the images obtained from the two cameras. Sometimes, due to issues with lighting, focus or camera angles, the software cannot map the speckles from one image to another, in this case, starting points are used to manually map the speckles between images. If the software cannot map enough points together, the data may have blank areas or even make analysis impossible. Next, the subset size and step size are chosen. The subset size controls the area of the image that is used to track the displacement between images, and it has to be large enough to ensure that there is a sufficiently distinctive pattern contained in the area used for correlation. The step size controls the spacing of the points that are analyzed during correlation. This means a step size of one will cause a correlation analysis to be performed at every pixel inside the area of interest [21]. For the bladder, subset sizes are usually kept below 60 depending on bladder size, speckle quality and focus while the step size is always one. An example of subset size selection can be seen in Figure 25 below.

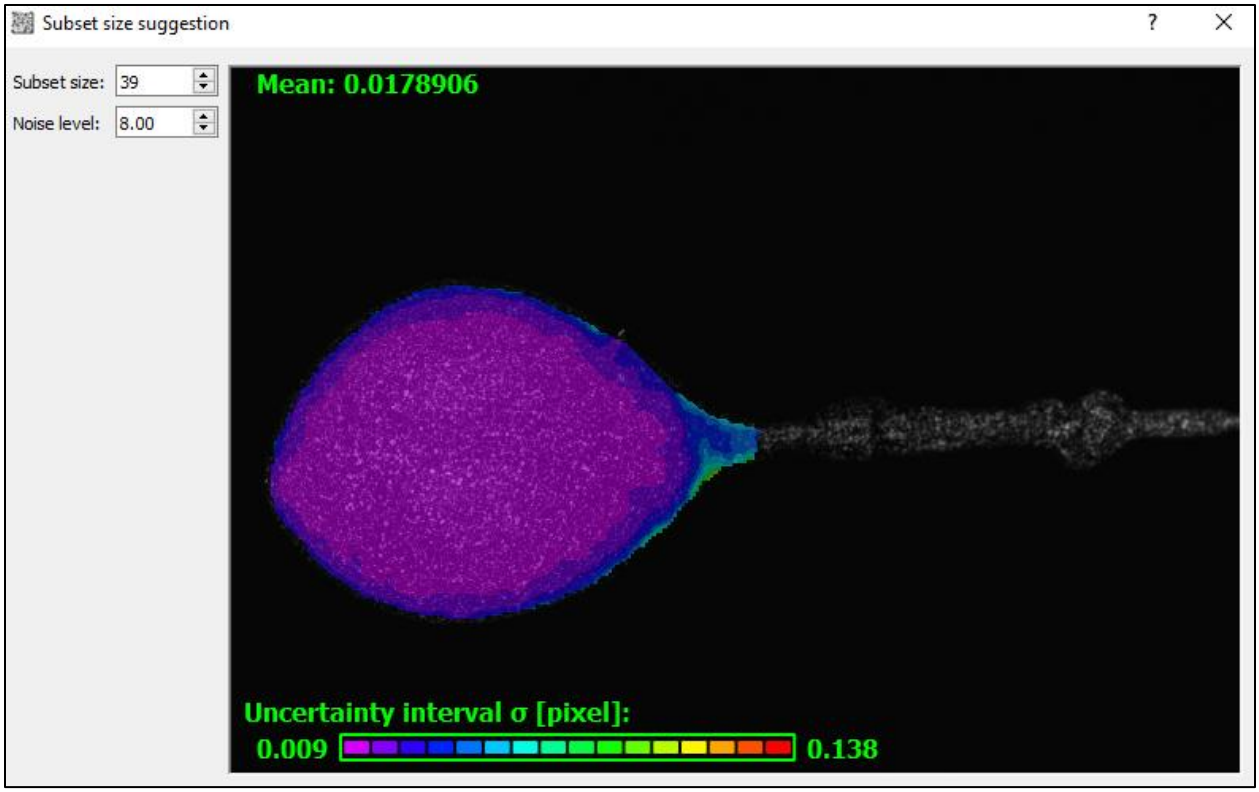

Figure 25 Subset size selection showing uncertainty intervals on bladder

With all parameters chosen, the speckled bladder images are now analyzed to create a 3D-reconstruction for each image taken, similar to Figure 13, and strain results are then obtained from these reconstructions software. The method used to obtain both results was explained in Section 2.2.

3.5 Methods: Virtual Field Method

The final step in analyzing the bladder was to determine the local stiffness values through the virtual field method. First, local wall thickness values are taken from the micro-CT results. This wall thickness results also include a point cloud which represents the geometry of the bladder and is pictured below in Figure 26. These results will be mapped to the DIC strain data.

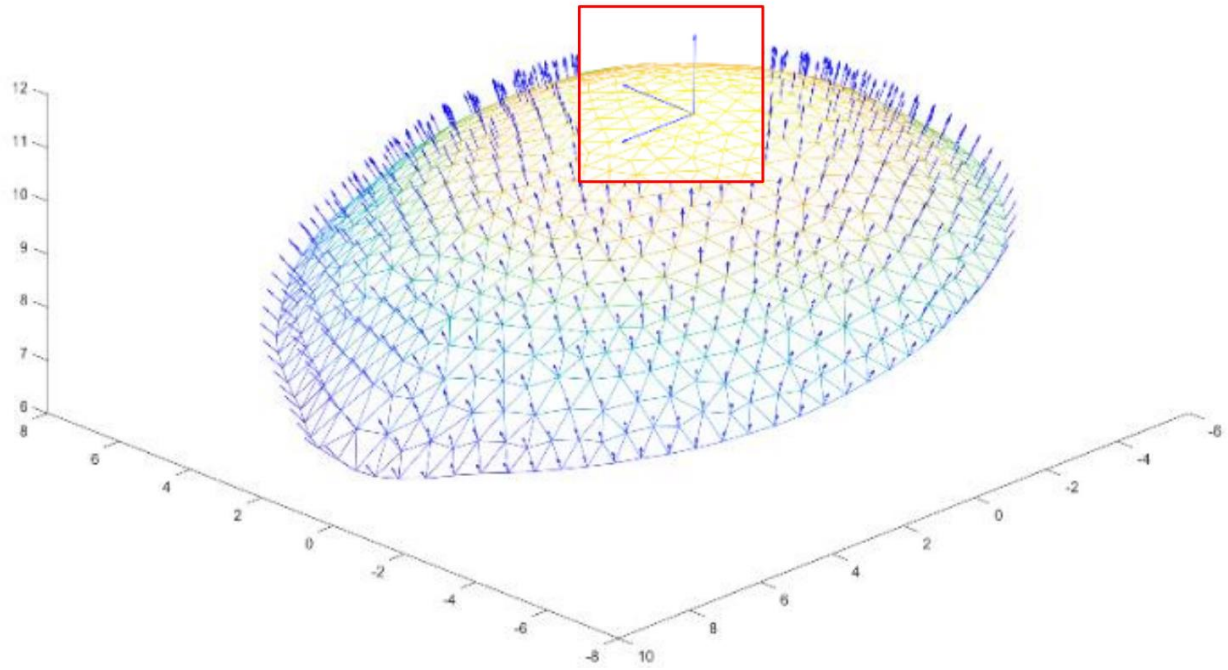

Figure 26 Point cloud with local coordinate system [25]

The strain values and wall thickness are then used to calculate stress values across the structure by using an assumed constitutive equation. Here we prescribed the material to be an incompressible Neo-Hookean material.

4.0 Results

As described in Section 3.2, the main experiments in this thesis were conducted on six bladders from young female rats between the ages of 3 and 4 months. Three rats treated with hypoxanthine for three weeks before harvesting and the other three were controls. This section presents and discusses the findings from these results along with results from the balloon testing.

4.1 Results: Micro-CT

4.1.1 Wall Thickness Data for Bladder

As mentioned in Section 3.3.2, each bladder was scanned at 7-mmHg and 35-mmHg and then analyzed to obtain a wall thickness color maps which are all shown in in Figures 27 through 32. Color maps were created for both the entire bladder and three bladder subsections, as described in Section 3.3.3 and illustrated in Figure 21. In this way, different ranges could be used for each segment to more clearly show the wall thickness. Table 3 and Figure 33 present the average wall thickness values for each bladder and the separate sections. Table 4 and Figure 34 present the inner bladder volume while Table 5 and Figure 35 provide the compliance values, calculated from bladder pressure and volume data obtained from micro-CT.

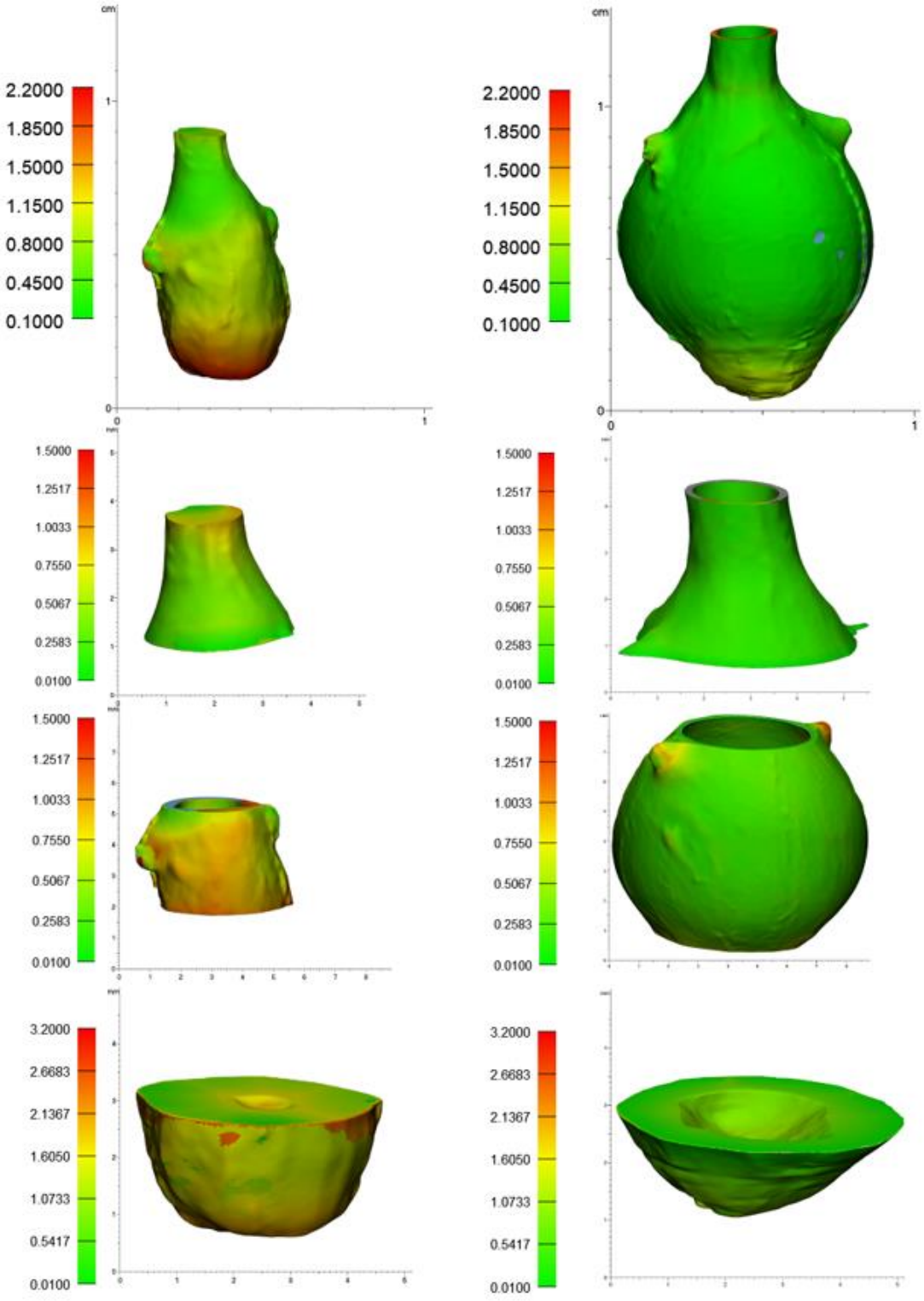

Figure 27 Control 1: Wall thickness color maps. Left column shows the 7mmHg results and right column shows 35mmHg results. From top to bottom rows, the segments are as followed: whole bladder, urethra segment, middle segment and dome segment. Note, there is a distinct color map legend for each row.

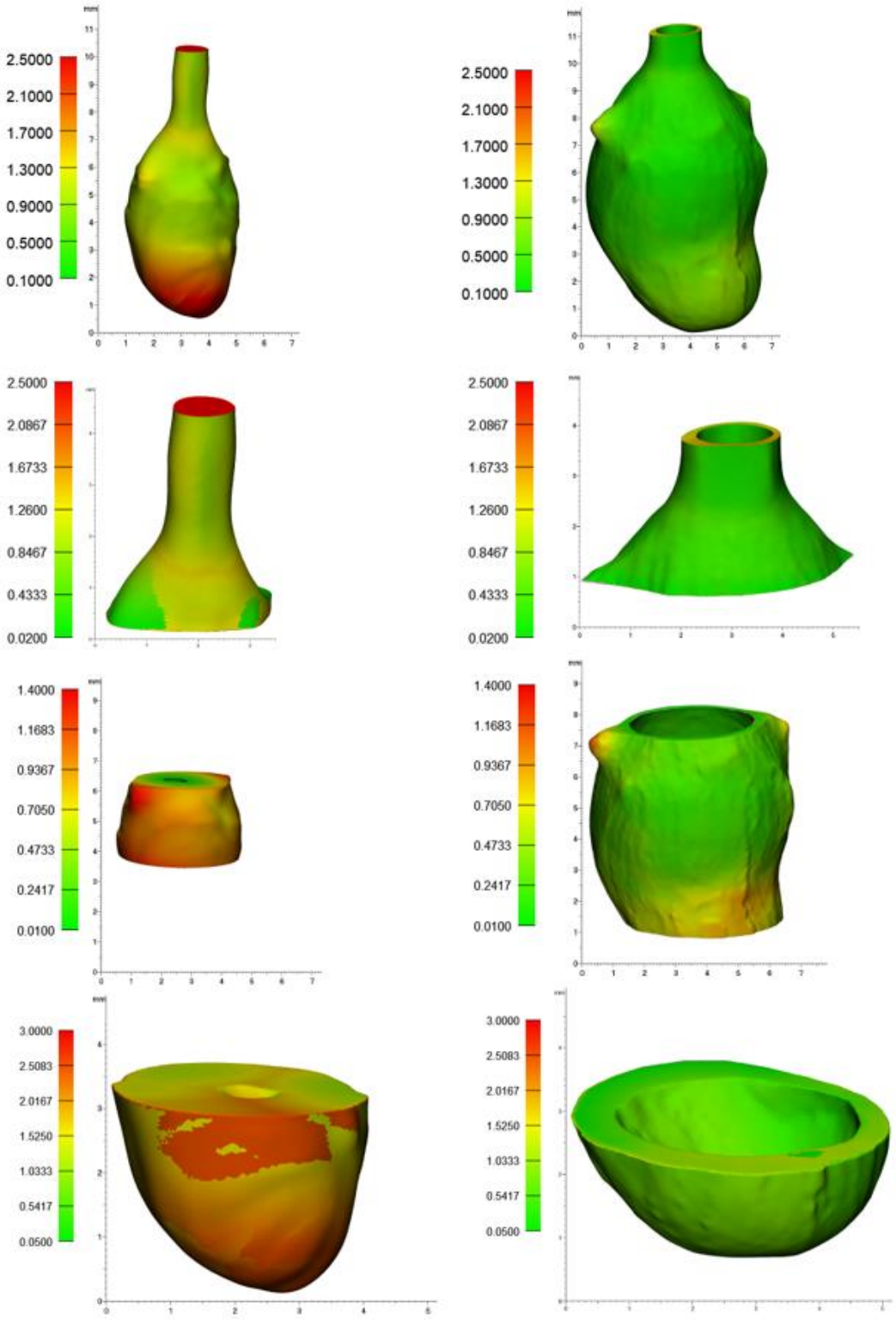

Figure 28 Control 2: Wall thickness color maps. Left column shows the 7mmHg results and right column shows 35mmHg results. From top to bottom rows, the segments are as followed: whole bladder, urethra segment, middle segment and dome segment. Note, there is a distinct color map legend for each row.

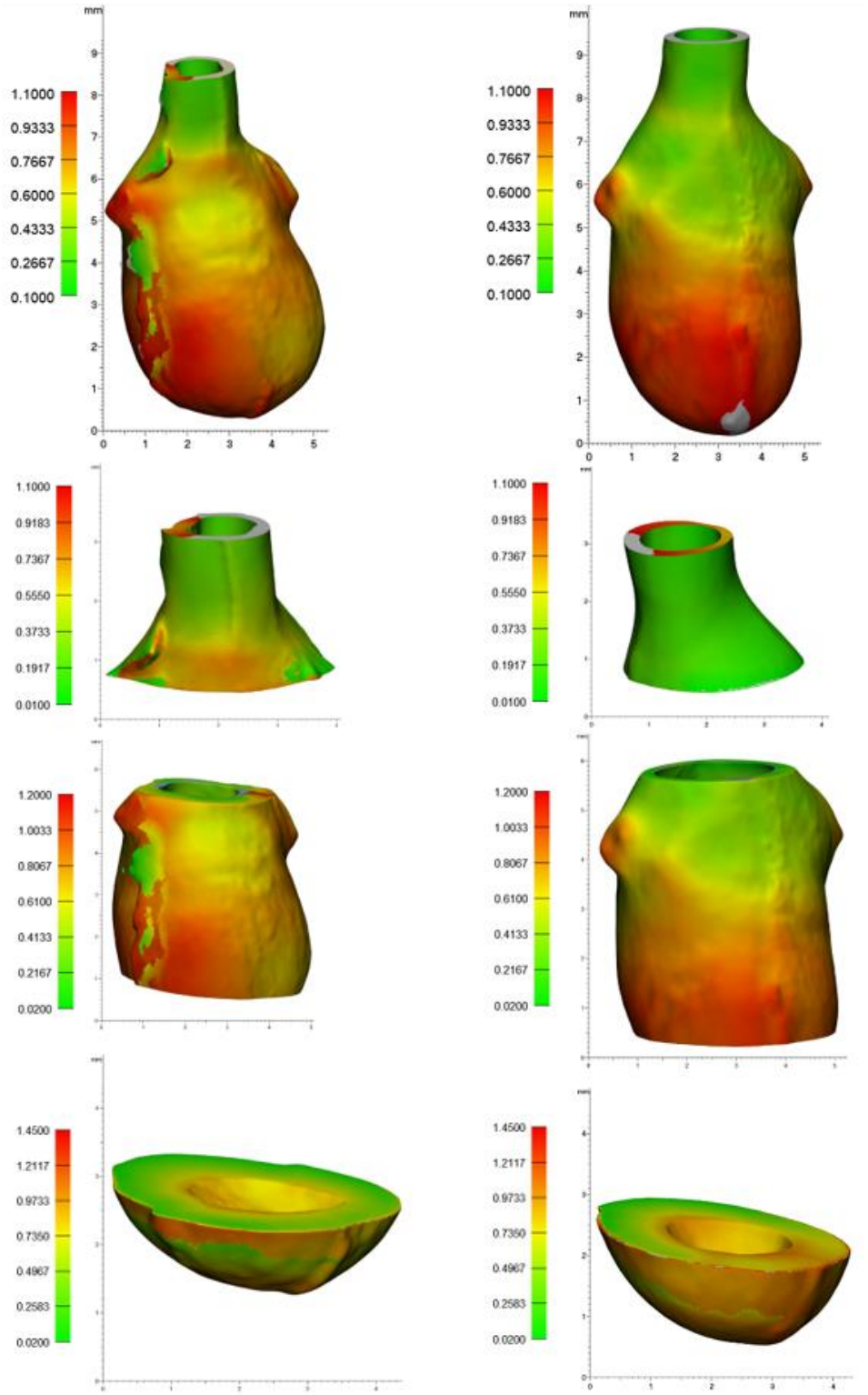

Figure 29 Control 3: Wall thickness color maps. Left column shows the 7mmHg results and right column shows 35mmHg results. From top to bottom rows, the segments are as followed: whole bladder, urethra segment, middle segment and dome segment. Note, there is a distinct color map legend for each row.

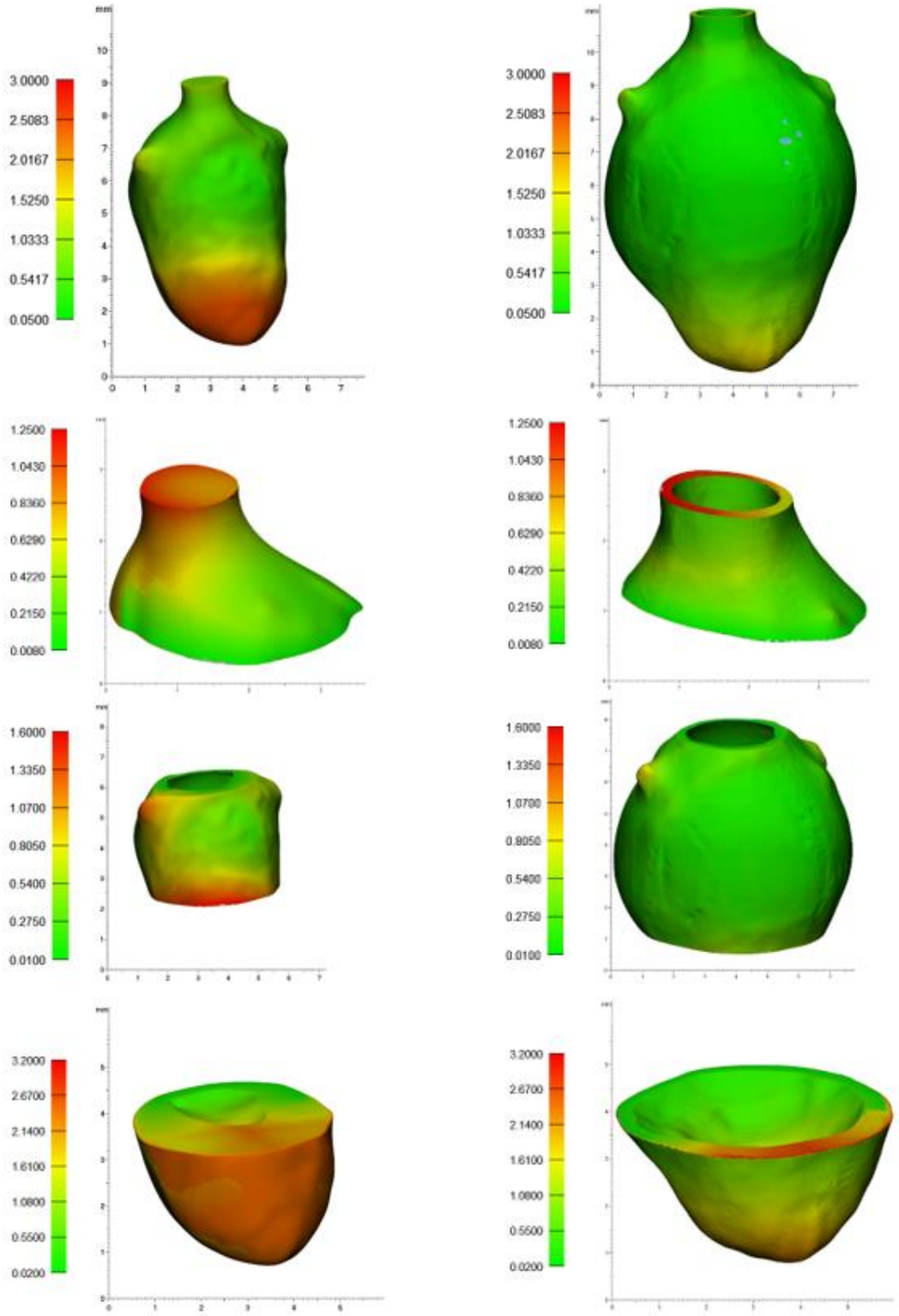

Figure 30 Treated 1: Wall thickness color maps. Left column shows the 7mmHg results and right column shows 35mmHg results. From top to bottom rows, the segments are as followed: whole bladder, urethra segment, middle segment and dome segment. Note, there is a distinct color map legend for each row.

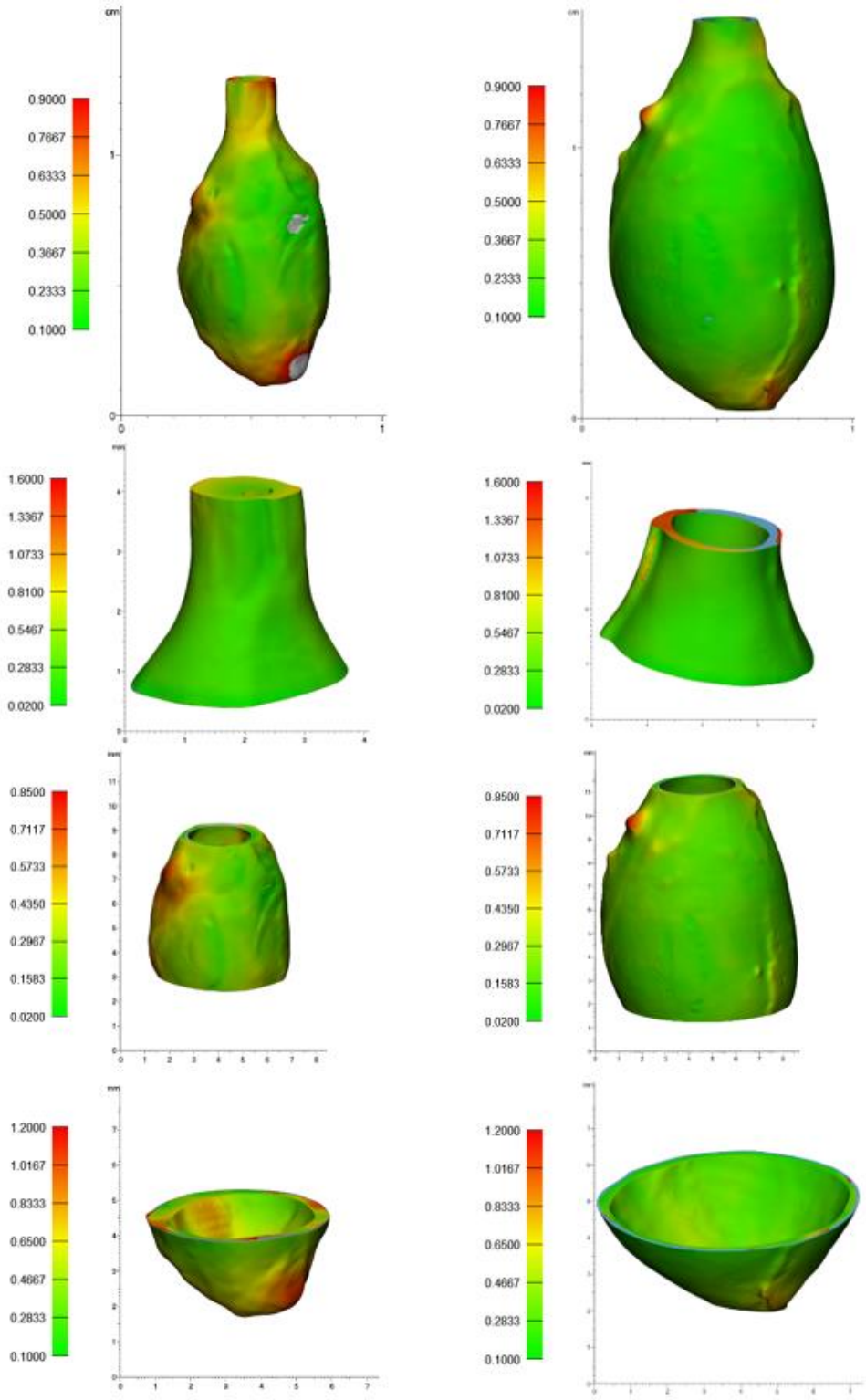

Figure 31 Treated 2: Wall thickness color maps. Left column shows the 7mmHg results and right column shows 35mmHg results. From top to bottom rows, the segments are as followed: whole bladder, urethra segment, middle segment and dome segment. Note, there is a distinct color map legend for each row.

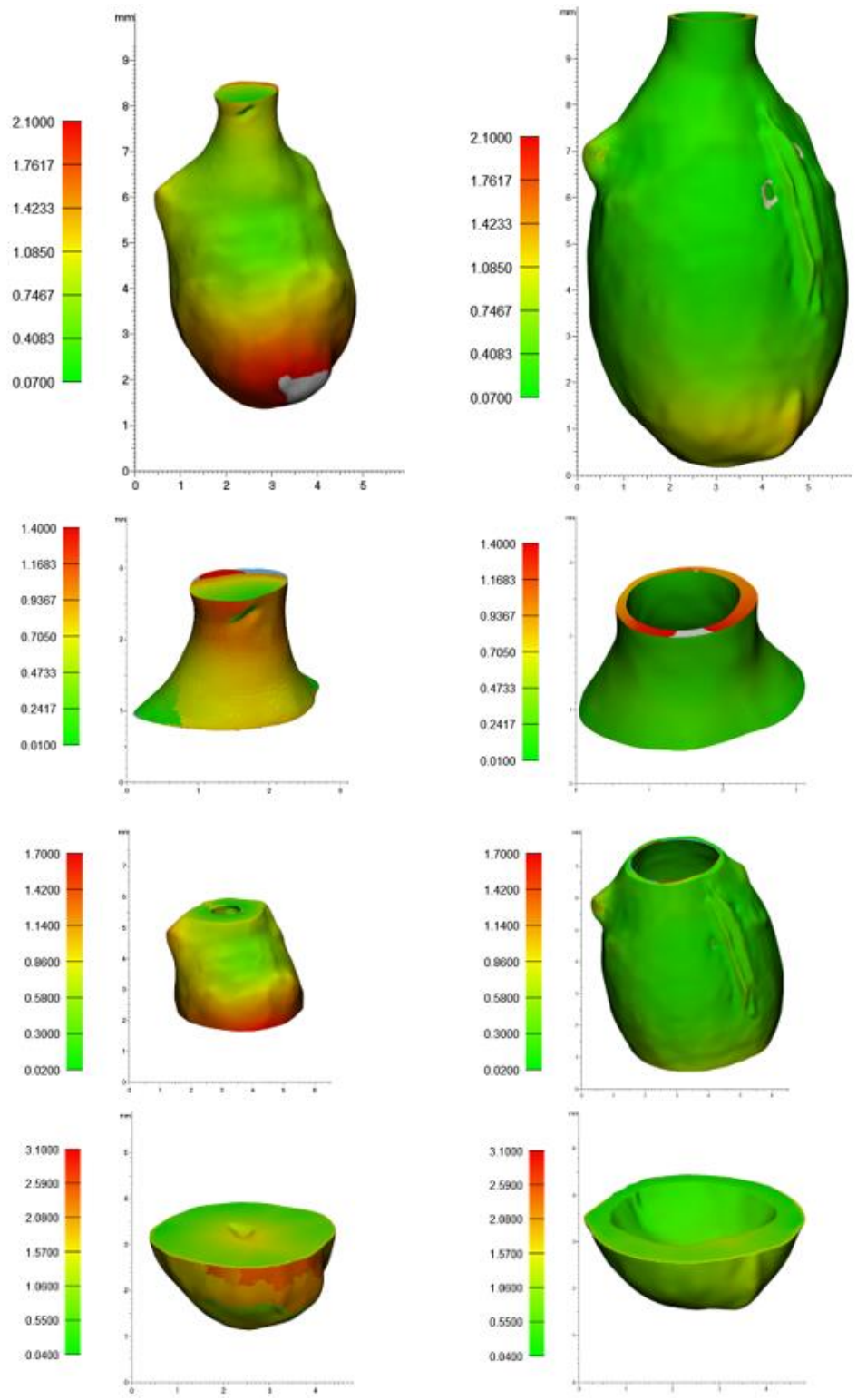

Figure 32 Treated 3: Wall thickness color maps. Left column shows the 7mmHg results and right column shows 35mmHg results. From top to bottom rows, the segments are as followed: whole bladder, urethra segment, middle segment and dome segment. Note, there is a distinct color map legend for each row.

Table 3 Average bladder wall thickness for whole bladder and bladder regions.

Average Wall Thickness Values (mm)								
	7mmHg Total	35mmHg Total	7mmHg Top	35mmHg Top	7mmHg Middle	35mmHg Middle	7mmHg Bottom	35mmHg Bottom
Control 1	0.94	0.26	0.54	0.18	0.63	0.18	1.63	0.61
Control 2	1.31	0.71	0.81	0.33	0.77	0.33	1.90	0.63
Control 3	0.71	0.63	0.37	0.28	0.70	0.59	0.61	0.78
Control Average	0.99 ± 0.30	0.53 ± 0.24	0.57 ± 0.22	0.27 ± 0.08	0.70 ± 0.07	0.37 ± 0.21	1.38 ± 0.68	0.67 ± 0.09
Treated 1	0.81	0.30	0.38	0.24	0.41	0.16	1.62	0.81
Treated 2	0.43	0.25	0.46	0.28	0.37	0.23	0.61	0.35
Treated 3	1.04	0.33	0.52	0.21	0.80	0.25	1.32	0.67
Treated Average	0.76 ± 0.31	0.29 ± 0.04	0.45 ± 0.07	0.24 ± 0.03	0.53 ± 0.24	0.22 ± 0.05	1.18 ± 0.52	0.61 ± 0.23

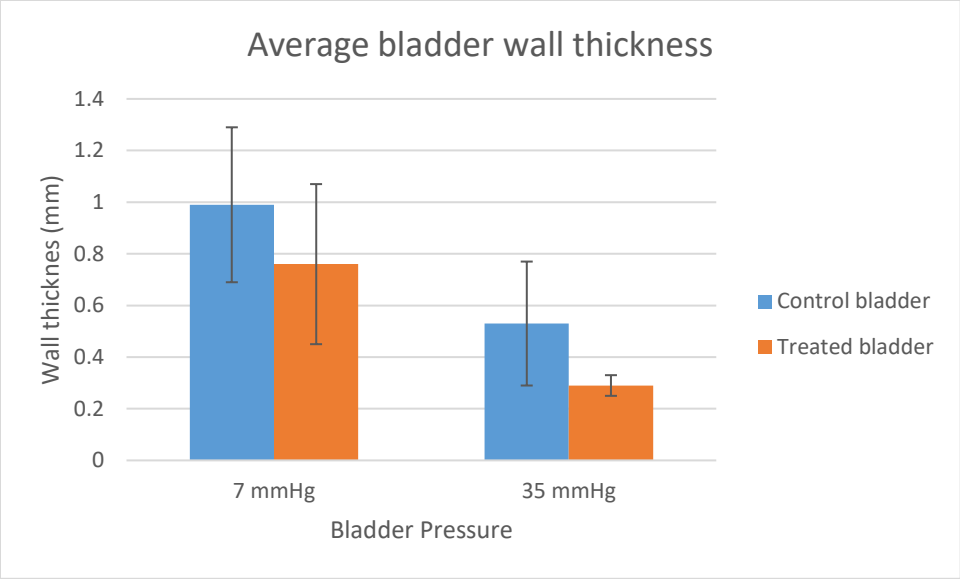

Figure 33 Average bladder wall thickness for whole bladder

Table 4 Bladder internal volume for whole bladder and bladder regions

Bladder volume (mm^3)		
	7mmHg Total	35mmHg Total
Control 1	15.5	282.03
Control 2	6.13	158.97
Control 3	26.97	42.94
Control Average	16.20 ± 10.44	161.31 ± 119.56
Treated 1	38.79	212.94
Treated 2	107.84	395.23
Treated 3	8.23	109.24
Treated Average	51.6 ± 51.03	239.14 ± 144.78

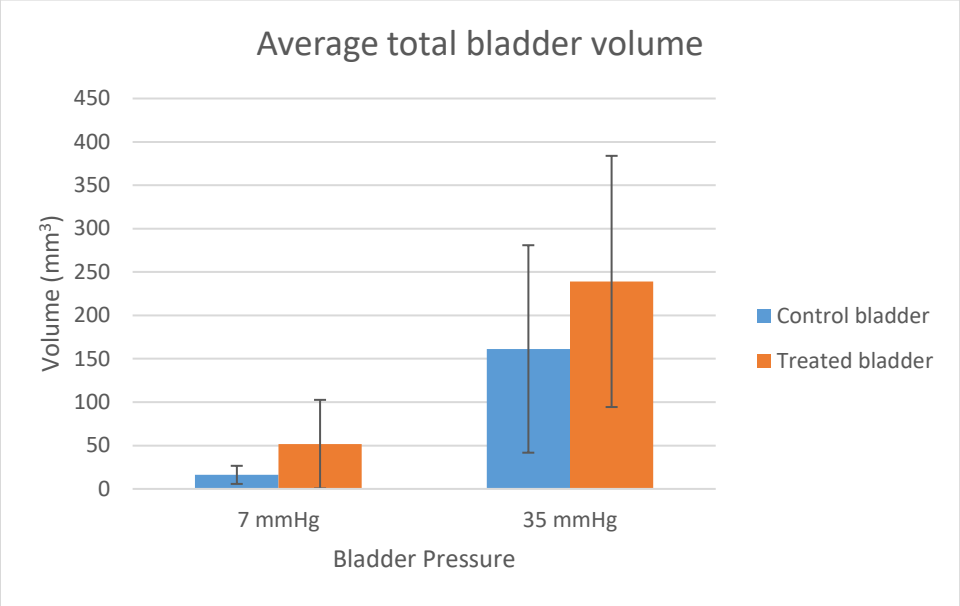

Figure 34 Average bladder volume

Table 5 Bladder compliance value

	Average compliance $(\frac{\Delta mm^3}{\Delta mmHg})$	
	Compliance	Average
Control 1	9.52	
Control 2	5.46	5.18 ±
Control 3	0.57	4.48
Treated 1	6.22	
Treated 2	10.26	6.70 ±
Treated 3	3.61	3.35

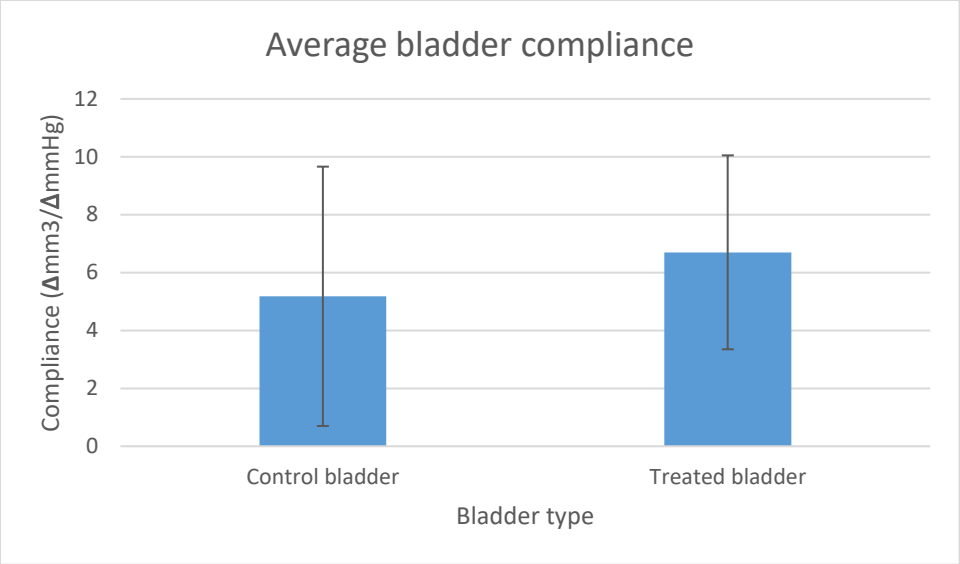

Figure 35 Average bladder complaince

4.1.2 Discussion of Results: Micro-CT

The results from the micro-CT provide a better understanding of the geometry of the bladder and provide local measurements that are then used for obtaining local stiffness values. From the results, as the pressure increases in the bladder, the wall thickness decreases especially closer to the urethra. This is visualized on the color maps in Figures 27 through 32 where the wall thickness closer to the urethra is consistently thinner than the dome of the bladder (opposite side of the urethra). On average, the control bladder has a thicker wall compared to the treated sample. Compliance was also calculated using the bladder volume values from Table 4 and the pressure. Compliance results are presented in Table 5. Both volume and compliance were greater, on average, in the treated cases. However, there are great regional differences in the filling process, it is important to consider the DIC data to understand the impact of treatment on bladder filling.

4.2 Results: Digital Image Correlation

4.2.1 Bladder Strain Fields

After speckling, the bladder was imaged and analyzed using digital image correlation to obtain local strain values of the bladder as shown in Figures 38 through 43. In Table 7, the mean strain values are provided for E_{xx} and E_{yy} along with the standard deviation. The mean strain value is calculated from several hundred thousand data points created from the speckling pattern. The E_{xx} strain refers to the strain in the X-direction and is illustrated using a balloon in Figure 36 while the E_{yy} strain refers to the strain the Y-direction and is illustrated on a balloon in figure 37.

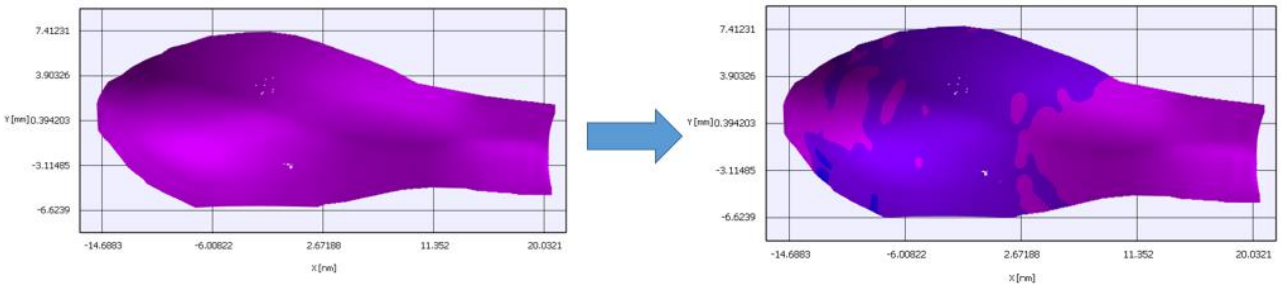

Figure 36 E_{xx} strain of a balloon when inflated from 5 mmHg (left) to 20 mmHg (right). Coordinate system shown on axis.

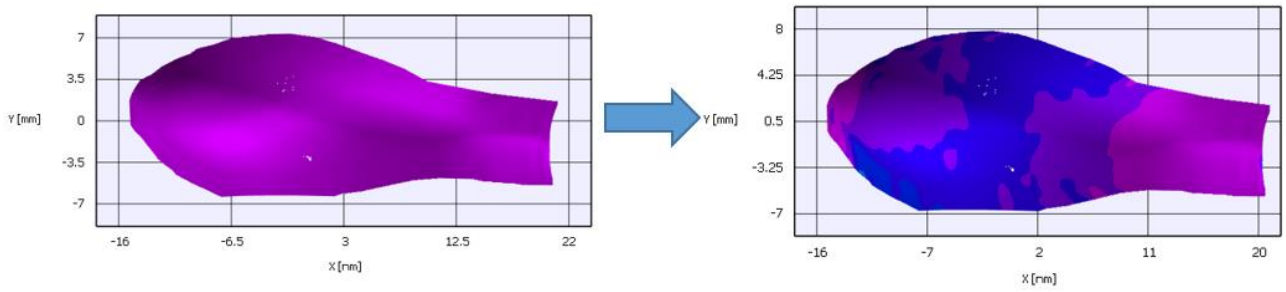

Figure 37 E_{yy} strain of a balloon when inflated from 5 mmHg (left) to 20 mmHg (right). Coordinate system shown on axis.

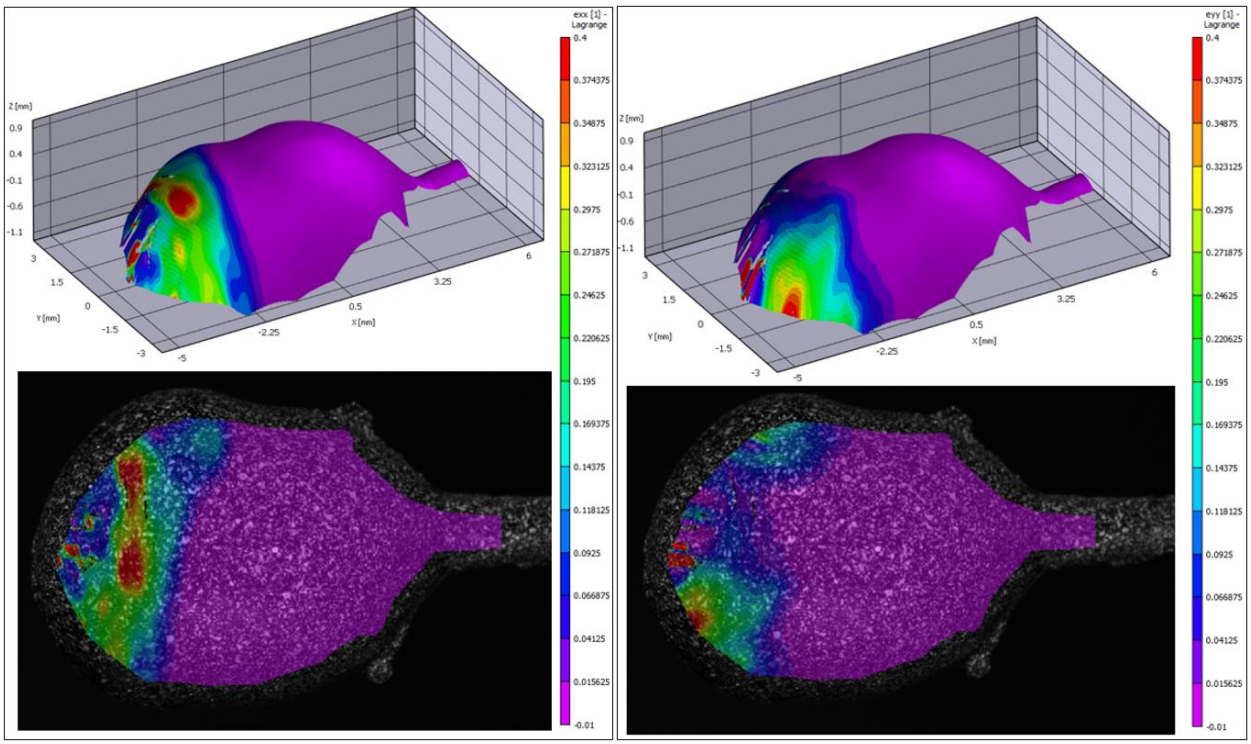

Figure 38 Control 1 strain color maps at 40mmHg. Left column represents Exx and right column represents Eyy. The top row shows a 3D-projection of the strain maps and the bottom row shows the strain results overlaid onto speckled bladder

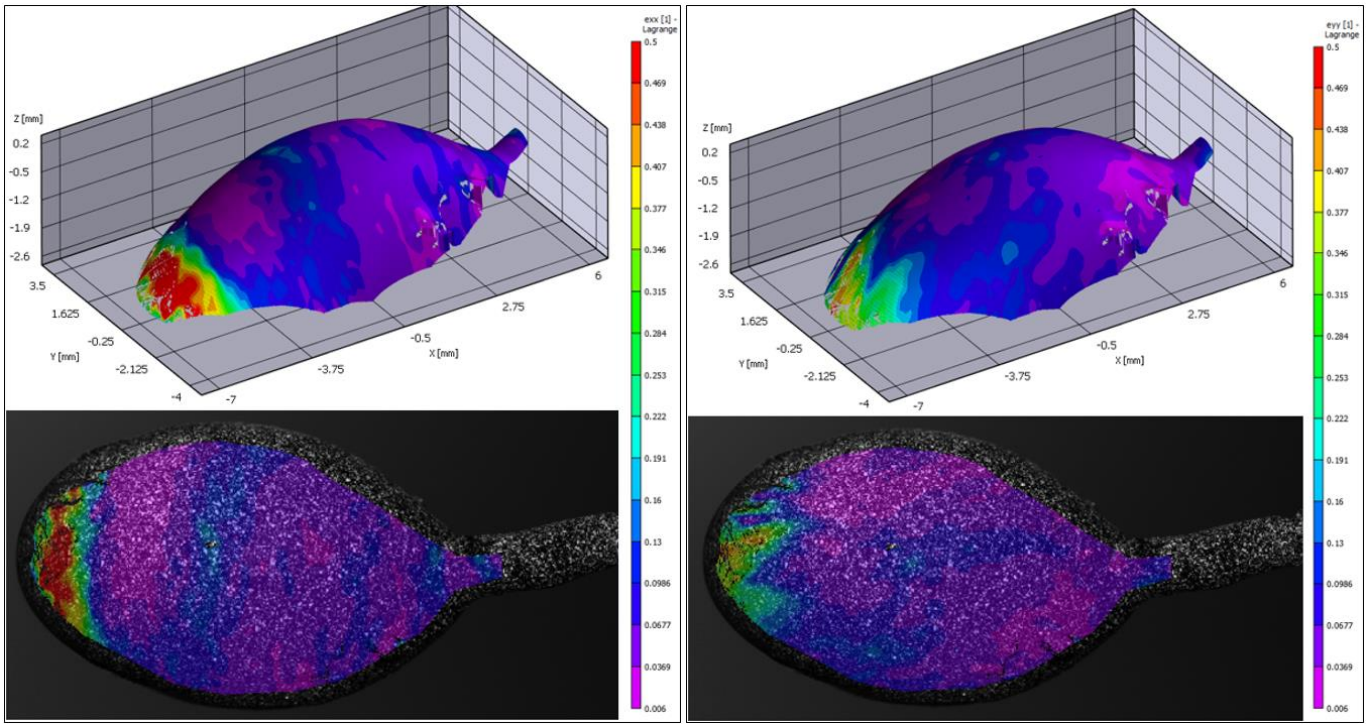

Figure 39 Control 2 strain color maps at 40mmHg. Left column represents Exx and right column represents Eyy. The top row shows a 3D-projection of the strain maps and the bottom row shows the strain results overlaid onto speckled bladder

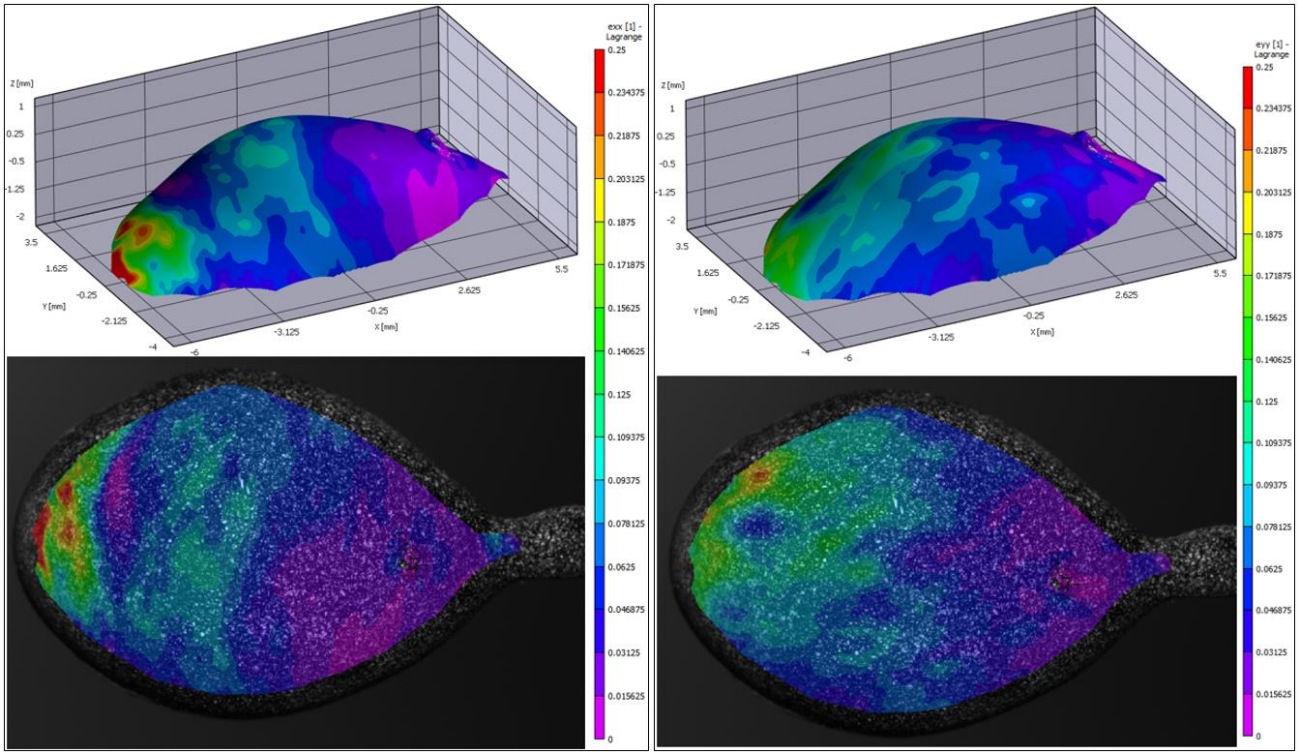

Figure 40 Control 3 strain color maps at 40mmHg. Left column represents Exx and right column represents Eyy. The top row shows a 3D-projection of the strain maps and the bottom row shows the strain results overlaid onto speckled bladder

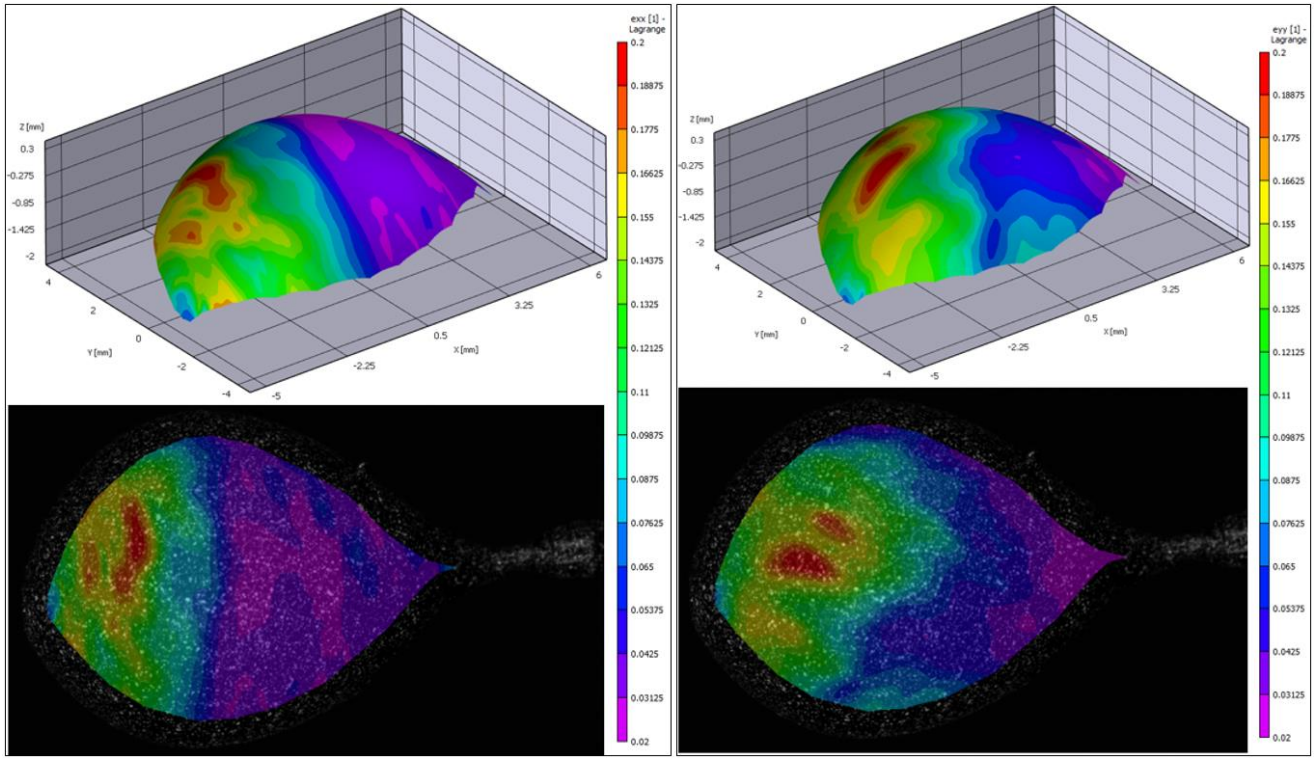

Figure 41 Treated 1 strain color maps at 40mmHg. Left column represents Exx and right column represents Eyy. The top row shows a 3D-projection of the strain maps and the bottom row shows the strain results overlaid onto speckled bladder

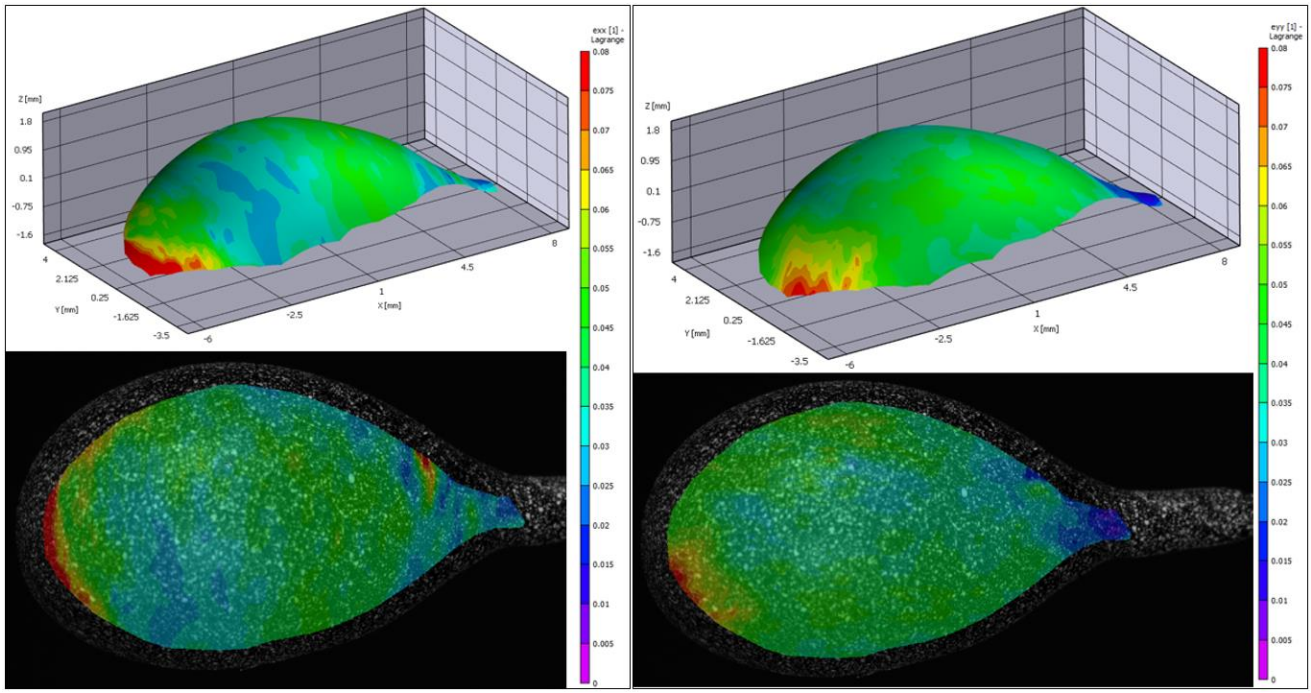

Figure 42 Treated 2 strain color maps at 40mmHg. Left column represents Exx and right column represents Eyy. The top row shows a 3D-projection of the strain maps and the bottom row shows the strain results overlaid onto speckled bladder

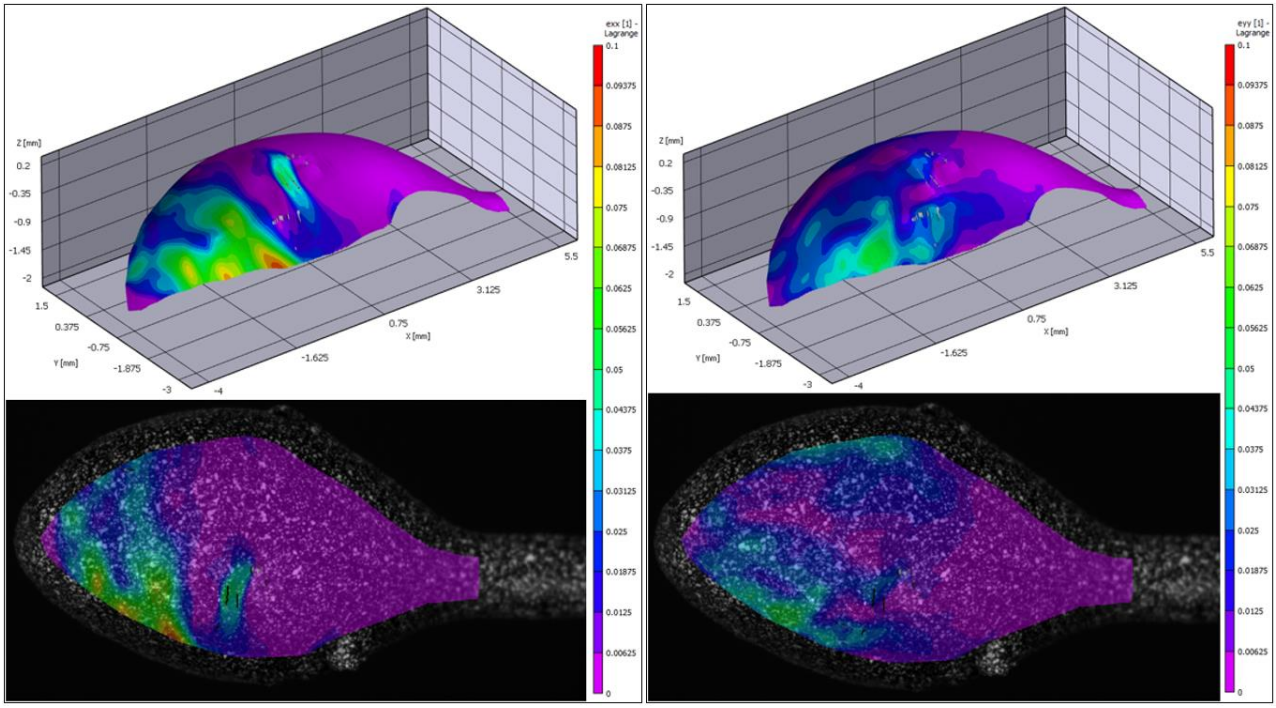

Figure 43 Treated 3 strain color maps at 40mmHg. Left column represents Exx and right column represents Eyy. The top row shows a 3D-projection of the strain maps and the bottom row shows the strain results overlaid onto speckled bladder

Table 6 DIC bladder mean strain results and standard deviations

Strain Values (mm/mm)		
	E_{xx} Strain	E_{yy} Strain
Control 1	0.05 ± 0.09	0.04 ± 0.20
Control 2	0.08 ± 0.08	0.07 ± 0.06
Control 3	0.06 ± 0.04	0.07 ± 0.04
Control Average	0.06 ± 0.07	0.06 ± 0.10
Treated 1	0.07 ± 0.05	0.09 ± 0.04
Treated 2	0.04 ± 0.01	0.04 ± 0.01
Treated 3	0.01 ± 0.02	0.01 ± 0.01
Treated Average	0.04 ± 0.03	0.05 ± 0.02

4.2.2 Discussion: Bladder Strain Field

From the results, the treated bladders seem to experience a slightly lower average E_{xx} strain of 0.04 ± 0.03 compared to the controls strain of 0.07 ± 0.05 and a lower average E_{yy} strain of 0.05 ± 0.02 compared to the controls strain of 0.09 ± 0.04. Although the treated bladders experienced lower strain, their inflation, shown in Section 4.1, was larger. Looking at the color maps, the minimum strains are close to zero implying that in these areas, very little deformation occurred, and that most of the deformation was localized to the dome areas of the bladder as seen in the color maps in Figures 38 through 43. Most of the bladders also experienced compression (negative

strain) in some areas. The color maps also showed that the strain was mostly localized near the dome of the bladder apart from treated 2, which experience some larger strains throughout. This finding suggests the bladder has heterogeneous properties that are not axisymmetric.

4.3 Representative Results for Bladder Wall Stiffness

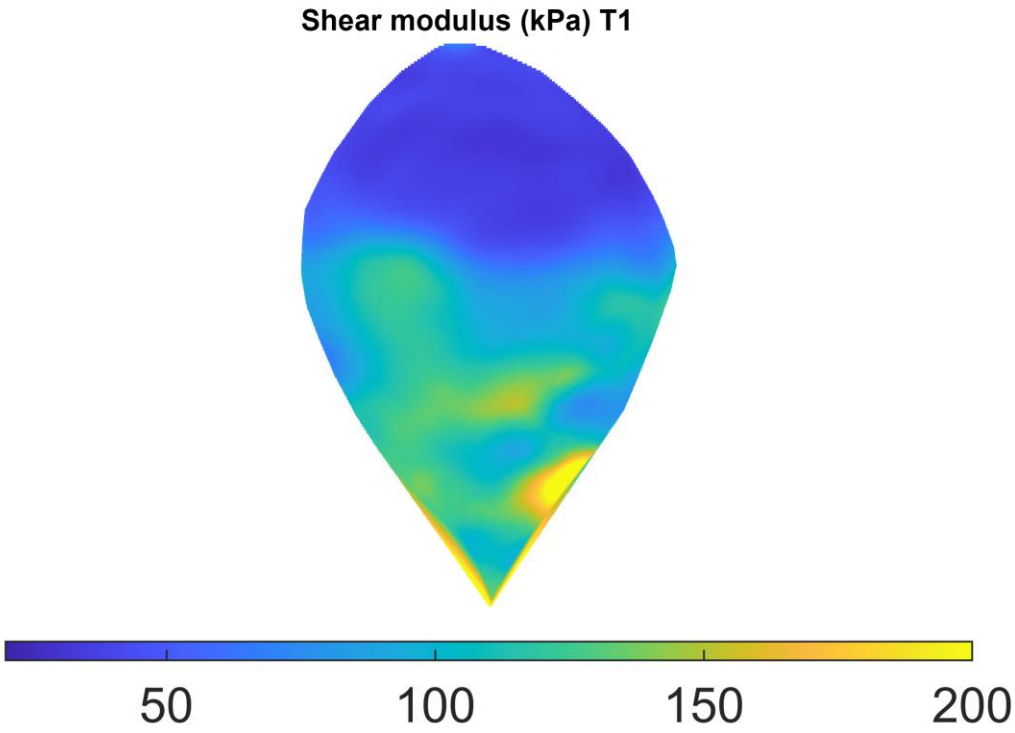

Figure 44 Treated 1 shear modulus

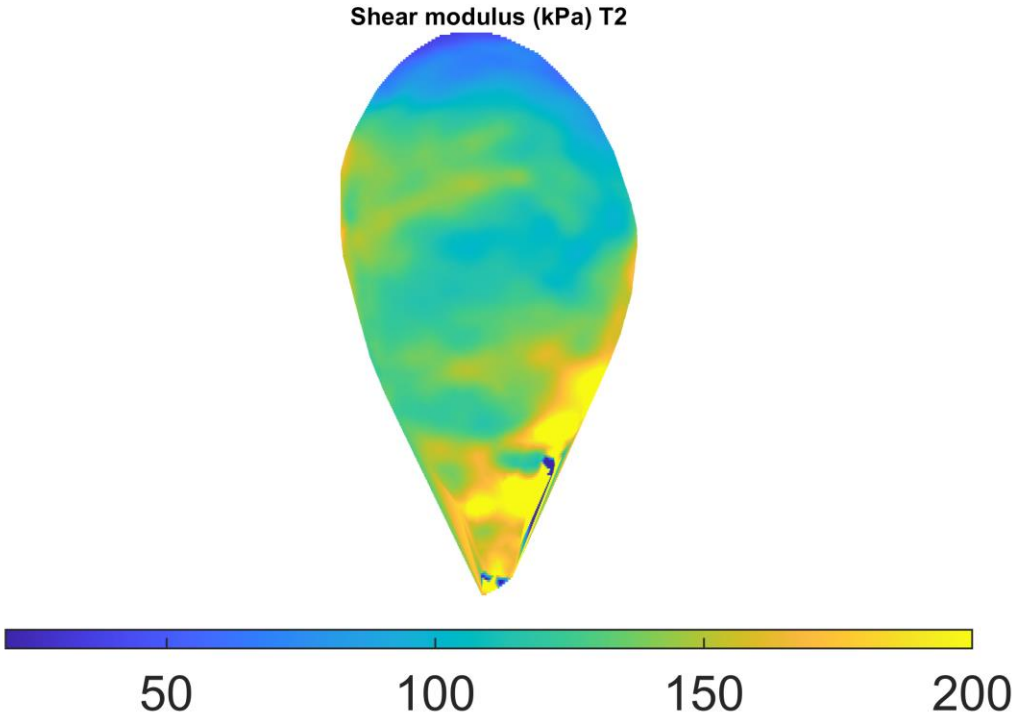

Figure 45 Treated 2 Shear modulus

4.3.1 Discussion of Results: Virtual Field Method

The local stiffness results, or shear modulus, are shown in Figures 45 and 46. These results were calculated by Dr. Avril's team using virtual field method (Section 3.5) using the DIC data and average wall thickness from the micro-CT data. Methods for the virtual field method are being further developed and because of this, results were only presented for treated 1 and treated 2. The shear modulus results show the stiffness closer to the urethra is greater. Higher shear modulus correlates to a stiffer material which would generally cause the bladder to experience lower strain in areas with a higher shear modulus. For both results, the dome of the bladder also has a low shear modulus which is consistent with the high strain area from the DIC results, though other factors, such as bladder geometry, impact this relationship.

These results on the rat bladder show lower elastic moduli than the study by Dahms *et al.* and discussed Section 1.2.1. There are several possible reasons for this. The current work is for whole bladder testing whereas the work of Dams *et al.* is for uniaxial testing. Further, the shear modulus acquired by Dr. Avril's group uses a neo-Hookean model that, as seen in Figure 47, will not capture the high strain stiffness of the bladder. We are currently developing this approach to include this exponential type response.

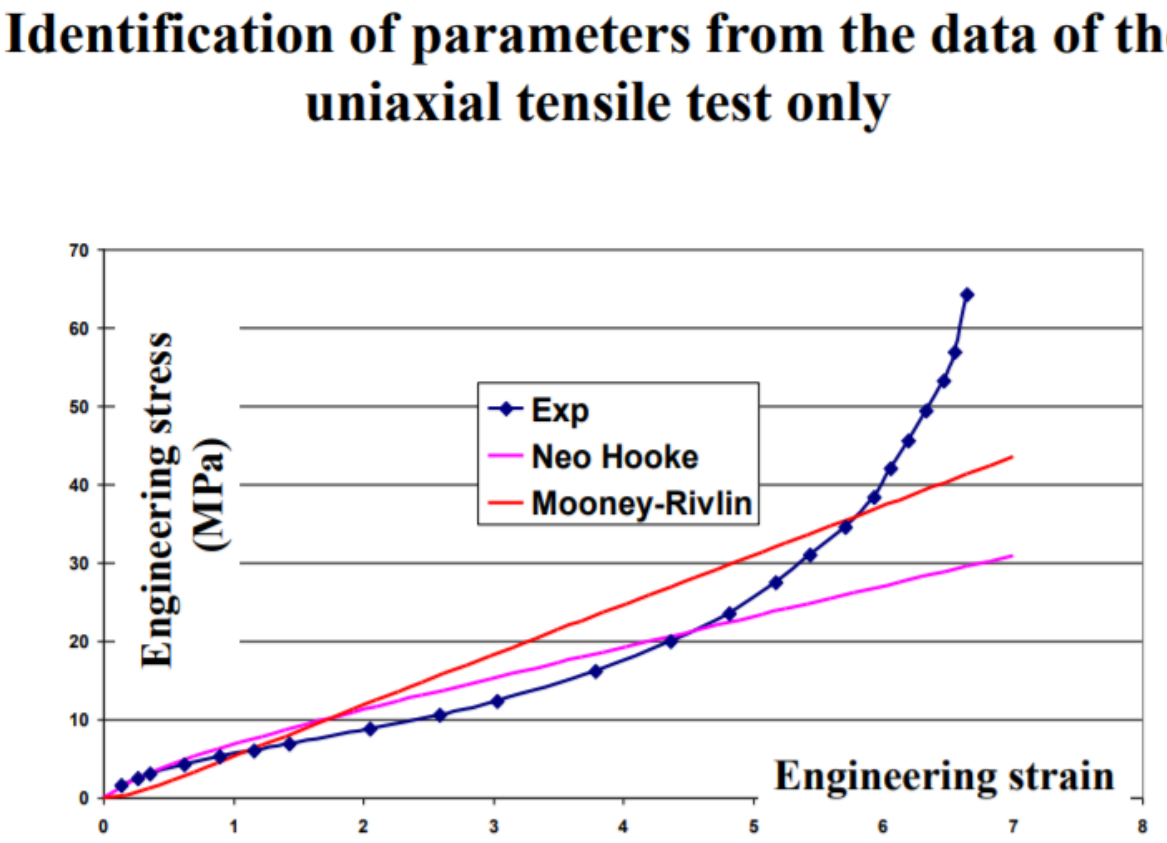

Figure 46 Stress-strain curve of uniaxial test done on aorta compared to neo-hookean and mooney-rivlin models [26]

5.0 Discussion

In this section, the experiments and results are discussed. These results have significance as they show that the bladders properties are heterogeneous and that there is a need to account for these differences when performing uniaxial testing, biaxial testing and biomechanical studies of the bladder wall. Limitations of the current work and future work are also discussed.

5.1 Implications and Limitations

The bladder has been studied by many researchers, but little research has been done on an entire rat bladder. Bladders have mostly been studied with the assumption that the properties are homogenous and with constant wall thickness. The results obtained in this thesis show that this is not the case, and that the bladder has heterogeneous properties and non-uniform thickness. This research also develops a pipeline for obtaining local results and stiffness maps. Knowing this, future research on bladders needs to consider the location of where the specimen originated. Without a proper catalog of where the bladder segment was obtained, results could be inconsistent since a stiffer part of the bladder may be compared to a less stiff section. Furthermore, the micro-CT shows that the dome of the bladder wall is much thicker than the urethra side and thins substantially as the bladder inflates. Finally, based on the DIC strain results, difference in E_{xx} and E_{yy} are not statistically significant which provides support for equi-biaxial testing of bladder specimens. Future studies can be used to explore this issue even further.

This study faced certain limitations that need to be addressed in future studies. When the bladder is subjected to sufficiently large loads, it can experience a creep which changes the geometry of the bladder. This creates a limitation in mapping the DIC data back to the micro-CT data for shear modulus calculations. In future studies, where the local wall thickness is used, it will be important to better understand these changes. Also, in the present study, only one set of stereo cameras were used, limiting the area of the bladder we can analyze. Finally, this study had a small sample size and further bladder testing needs to be conducted to determine statically significant results.

5.2 Future Work

The work presented in this thesis provides a protocol for obtaining mechanical properties of the bladder. Further development of this protocol, and an increase in the sample size, will enable analysis of statistically difference in behavior between treated and control bladders. Also, the addition of more cameras in the DIC tests would allow for an entire 360-degree view of the bladder to be captured and analyzed. Furthermore, the use of the virtual field method is illustrated in this thesis and further development of it will provide more information on the bladder behavior. In the future, the virtual field method can be used to develop a 360-degree model of the bladder's mechanical properties. After the tests presented in this thesis are conducted, the bladders wall structure can be analyzed to see its mechanical response and better understand its behavior. Finally, more research areas can be developed to understand, for example, the behavior of the urethra when opening and closing and the impact it has on bladder mechanics.

5.3 Conclusion

The bladder is a highly compliant organ that has been shown to decrease in efficiency with age. Most previously conducted research employs uniaxial or biaxial testing and generally assumed the bladder has homogeneous properties. The objective of the thesis was to develop and implement a method to analyze whole rat bladders noninvasively and evaluate the mechanical properties. The bladder was first imaged using micro-CT and this data was analyzed to determine the wall thickness and bladder shape. Next, the bladder was analyzed using digital image correlation which produced a strain field for the bladder. The strain data and wall thickness data were analyzed by our collaborators using a virtual field method to produce the materials stiffness assuming a Neo-Hookean model. The results showed that the bladder has heterogeneous properties. Further research will be conducted to address limitations and further advance these studies so that they potentially can aid in the development of new treatment for loss of bladder functionality with age.

Bibliography

[1] Kershen, R. T., Azadzoi, K. M., and Siroky, M. B., "Blood Flow, Pressure and Compliance in the Male Human Bladder," *J. Urol.*, vol. 168, no. 1, pp. 121–125, 2002.

[2] Kaname Ameda, R. J. B and S. V. Y., Maryrose Sullivan P., "Uurodynamic characterization of nonobstuctive voiding dysfunction in symptomatic elderly men" *J. Urol.*, vol. 162, pp. 142–146, 1999.

[3] Madersbacher, Stephan et al. "Interrelationships of Bladder Compliance with Age, Detrusor Instability, and Obstruction in Elderly Men with Lower Urinary Tract Symptoms." *Neurourology and Urodynamics* 18.1 (1999): 3–13. *Neurourology and Urodynamics*. Web

[4] M. B. Siroky, "The aging bladder.," *Rev. Urol.*, vol. 6 Suppl 1, pp. S3–S7, 2004.

[5] Andersson, K.E. and Wein, A. J., "Pharmacologic management of lower urinary tract storage and emptying failure.," in *Campbell -Walsh Urology, 11th Edition*, 10th editi., A. J. Wein, L. R. Kavoussi, A. W. Partin, and C. A. Peters, Eds. Philadelphia, PA: Elsevier, 2011, pp. 1836–1874.

[6] Palmer, C.J. and Choi, J.M., "Pathophysiology of Overactive Bladder: Current Understanding," *Curr. Bladder Dysfunct. Rep.*, vol. 12, no. 1, pp. 74–79, 2017.

[7] Cheng, F. *et al.*, "Layer-dependent role of collagen recruitment during loading of the rat bladder wall," *Biomech. Model. Mechanobiol.*, vol. 17, no. 2, pp. 403–417, 2018.

[8] Alexander, R.S. Mechanical properties of urinary bladder. Am. J. Physiol. Leg. Content 220, 1413–1421 (1971).

[9] Chantereau, P. et al. Mechanical properties of pelvic soft tissue of young women and impact of aging. Int. Urogynecol. J. 25, 1547–1553 (2014)

[10] Dahms, S.E., Piechota, H.J., Dahiya, R., Lue, T.F. & Tanagho, E.A. Composition and biomechanical properties of the bladder acellular matrix graft: Comparative analysis in rat, pig and human. Br. J. Urol. 82, 411–419 (1998)

[11] Gloeckner, D.C., Sacks, M., Chancellor, M. & DeGroat, W. Active and passive biaxial mechanical properties of urinary bladder wall. In: Proceedings of the First Joint BMES/ EMBS Conference (IEEE, 1999).

[12] Morales-Orcajo, Enrique, Tobias Siebert, and Markus Böl. "Location-Dependent Correlation between Tissue Structure and the Mechanical Behaviour of the Urinary Bladder." *Acta Biomaterialia* 75 (2018): 263–278. *Acta Biomaterialia*. Web.

[13] Hounsfield, G.N. (1973) Computerized transverse axial scanning (tomography). 1. Description of system. Br. J. Radiol. 46, 1016–1022

[14] Holdsworth, David W., and Michael M. Thornton. "Micro-CT in Small Animal and Specimen Imaging." *Trends in Biotechnology* 1 Aug. 2002. *Trends in Biotechnology*. Web.

[15] "SKYSCAN 1272." *Bruker*, www.bruker.com/en/products-and-solutions/microscopes/3d-x-ray-microscopes/skyscan-1272.html

[16] "Literature Survey." *Image Correlation for Shape, Motion and Deformation Measurements: Basic Concepts, Theory and Applications*, by Michael Albert Sutton et al., Springer, 2009, pp. 1–3.

[17] "Introduction to Image Matching." *Image Correlation for Shape, Motion and Deformation Measurements: Basic Concepts, Theory and Applications*, by Michael Albert Sutton et al., Springer, 2009, pp. 81-83.

[18] Liu, Xiao Yong et al. "A Self-Adaptive Selection of Subset Size Method in Digital Image Correlation Based on Shannon Entropy." *IEEE Access* 8 (2020): 184822–184833. *IEEE Access*. Web.

[19] Strain Calculation in Vic-3D. Correlated Solution, 11 Oct. 2016, www.correlatedsolutions.com/supportcontent/strain.pdf.

[20] Farzaneh, Solmaz, Olfa Trabelsi, and Stéphane Avril. "Inverse Identification of Local Stiffness across Ascending Thoracic Aortic Aneurysms." Biomechanics and Modeling in Mechanobiology 18.1 (2019): 137–153. Biomechanics and Modeling in Mechanobiology. Web.

[21] Vic-3D Software Manual, correlated Solution, 08 July 2019,http://www.correlatedsolutions.com/installs/Vic-3D-2010-manual.pdf

[22] Rubod, C. et al. "Biomechanical properties of vaginal tissue. Part 1: new experimental protocol." *The Journal of urology* 178 1 (2007): 320-5; discussion 325 .

[23] Jokandan, Maryam Sami et al. "Bladder Wall Biomechanics: A Comprehensive Study on Fresh Porcine Urinary Bladder." *Journal of the Mechanical Behavior of Biomedical Materials* 79 (2018): 92–103. *Journal of the Mechanical Behavior of Biomedical Materials*. Web.

[24] “Introduction to Image Matching.” *Image Correlation for Shape, Motion and Deformation Measurements: Basic Concepts, Theory and Applications*, by Michael Albert Sutton et al., Springer, 2009, pp. 150-151.

[25] Grimberg, Adrien” Summer *2021 internship report: mechanical characterization of biological tissues”* Summer internship report, University of Pittsburgh, Pittsburgh, PA 19 Aug, 2021. Print

[26] Avril, Stephane Ph.D. “Basics of Continuum Mechanics for Soft Tissues.” Mines Saint-Etienne. Received 19 Sept. 2021. Course Lecture